



DEPARTMENT OF INFORMATICS

TECHNISCHE UNIVERSITÄT MÜNCHEN

Master's Thesis in Informatics

**Spotlight based Instrument Navigation in
3D for Retinal Surgery**

Felix Hennerkes



DEPARTMENT OF INFORMATICS

TECHNISCHE UNIVERSITÄT MÜNCHEN

Master's Thesis in Informatics

Spotlight based Instrument Navigation in 3D for Retinal Surgery

Lichtbasierte Instrumentennavigation in 3D für Augenoperationen

Author:	Felix Hennerkes
Supervisor:	Prof. Dr. Nassir Navab
Advisor:	Dr. Mingchuan Zhou
Additional Advisor:	Dr.-Ing. M. Ali Nasser
Submission Date:	30.09.2020

I confirm that this master's thesis in informatics is my own work and I have documented all sources and material used.

Munich, 30.09.2020

Felix Hennerkes

Abstract

Retinal surgery is a very complicated and challenging task for an experienced eye surgeon. Robot-assisted image-guidance is one of the novel and promising technologies that may increase the human capabilities during microsurgery. In this thesis the possibility of using a spotlight with a cone-shaped light beam to localize the instrument inside the eye is analyzed. Additionally, a concept including three spotlights is evaluated.

First, a short overview of the related work and the proposed method is presented.

After introducing the concept, the mathematical background is used to show that the theoretical error introduced by the utilized method is negligible. The concept is further tested using a simulation, where the localization is applied under different conditions.

During the tested movements, the version with a single spotlight is able to achieve an average error of less than 0.05 mm with a maximum error of less than 0.15 mm. The version with multiple spotlights improves the average error to less than 0.03 mm and the maximum error to below 0.09 mm.

Additionally a direct correlation between the intensity of the spotlight and the error is observed.

Contents

Abstract	iii
1 Introduction	1
2 State of the Art	3
2.1 Optical Coherence Tomography	3
2.2 Camera	3
2.3 Structured Light	4
3 Concept	6
3.1 Overview	6
3.2 Single Spotlight Localization	6
3.3 Multiple Spotlight Localization	8
4 Theoretical Background	10
4.0.1 Pattern Reconstruction	10
4.1 Cone-Sphere Intersection	12
4.2 Cone-Plane Intersection	13
4.3 Camera Projection	16
4.4 Ellipse to Cone Reconstruction	17
5 Simulation	20
5.1 Overview	20
5.2 Blender Setup	20
5.3 Localization Algorithm	22
5.4 Position Reconstruction with Multiple Spotlights	24
5.5 Calibration	26
6 Tests	27
6.1 Overview	27
6.2 Ellipse-based Vertex Reconstruction	27
6.2.1 Overview	27
6.2.2 Perpendicular Positioning	28

Contents

6.2.3	Angled Positioning	30
6.3	Projection and Vertex Reconstruction	31
6.3.1	Perpendicular Positioning	31
6.4	Linear Movement	32
6.4.1	Overview	32
6.4.2	Result	34
6.5	Helix Movement	39
6.5.1	Result	39
6.6	Light Intensity	45
6.6.1	Results	46
6.7	Deformed Surface	51
6.7.1	Results	51
6.8	Curvature	53
6.8.1	Results	53
6.9	Calibration	53
7	Conclusion	54
7.0.1	Concepts	54
7.0.2	Simulation	54
7.0.3	Results	55
7.0.4	Future Work	55
List of Figures		56
List of Tables		58
Bibliography		59

1 Introduction

In their World Report on Vision published in 2019, the World Health Organization (WHO) estimates that around 2.2 billion people have vision impairments. The WHO further estimates that around 1 billion of those vision impairments could have been prevented given appropriate treatment, or still can be treated. They also highlight the lack of access to treatments especially in poorer and less developed countries and name the lack of trained human resources as one of the main challenges [5].

Due to limitations in the human motorical capabilities, retinal microsurgery is one of the most challenging surgical tasks. The challenges include the need for highly precise movements in a very small and fragile environment, which is also difficult to access. It is further hindered by poor visibility, movements of the patient and physiological hand tremor of the surgeon [10].

To overcome the motorical limitations, researchers introduced robots designed to provide highly precise instrument movements, while filtering out hand tremors. Clinical trials have already shown that the usage of such robotic assistance can greatly improve the results of the operation. Robot assisted surgery is also envisioned to decrease the work intensity and with that increase the working lifetime of a surgeon [14].

Due to the increased accuracy also, new procedures become possible. In the long run robot assistance is envisioned to make eye surgeries more affordable and increase their availability.

Introducing more autonomy to the assisting robots has the prospect to further increase the advantages of robot assisted surgeries. An important step towards more autonomy for the retinal microsurgery is not relying on human vision to localize the instrument within the eye. This would allow the robot to perform specified movements without human real-time input or can be used as a further assistance to the surgeon.

The instrument localization for retinal surgery has been a research topic for a few years and different possible approaches are published. These approaches can roughly be categorized by their utilized localization methodology into optical coherence tomography-based (OCT), camera image-based and structured light-based localization.

In this thesis a localization concept using structured light is evaluated using a simulation. The concept is based on a previous work [22], where the structured light is used to derive the tip to surface distance of the instrument, with very promising results. The main contribution of this thesis is to analyze the possibility to use this concept to

derive not only the tip-to-surface distance but the full position including the rotation of the instrument. Additionally, an adapted concept with multiple spotlights attached to the instrument is evaluated.

In the next chapter an introduction into the existing methods for the instrument localization for retinal surgery is given. Afterwards the concept evaluated in this thesis is presented. The required theoretical background is listed in chapter 4. The concept is tested using a simulation described in chapter 5. Finally, the results of the simulation are presented in chapter 6.

2 State of the Art

2.1 Optical Coherence Tomography

Optical Coherence Tomography (OCT) is a 3D imaging technique that utilizes light with a very high wavelength that can penetrate the surface. Based on the reflections of the light, caused by features below the surface, OCT constructs a high-resolution spatial image of the scanned tissue [15].

It is often used by ophthalmologists to obtain a spatial image of the retina. Compared to other three-dimensional imaging techniques OCT has the advantages of providing a very high resolution without using harmful radiation.

In [20] and [21] deep learning is used to segment the instrument in the OCT image for subretinal injections. The segmented instrument is used in [18] to derive the 6 degrees of freedom pose with a modified iterative closest point algorithm and the tip position [19].

In [17] a custom made OCT probe is used for image guidance and in [4] the depth of subretinal needle injections are determined using real-time OCT imaging.

In these different applications, the OCT-based guidance performed very good, but due to the small perception range, the technique is limited to a guidance within a confined area. This makes it unsuitable for localization tasks within a bigger area inside the eye.

Its advantages can still be utilized by combining a OCT based localization with a localization mechanism that can operate in a less confined area.

2.2 Camera

The camera-based systems typically use a microscope and a monocular or binocular camera setup to capture the retina through the pupil. The main differences lie in the usage of different algorithms to estimate the instrument position based on the captured images.

In [7] localization method based on regression forests to track the position and orientation of the instrument is introduced. In [8] a similar concept is used with the addition of modeling the instrument as an articulated object.

[1] models the instrument as a conditional random field and tracks each part of the instrument separately. By the known properties and relations between the parts, the captured image is then used to localize the instrument through the scale and location of the individual parts.

Different from the other two approaches in [6] a stereo microscope setup is used. The location of the spotlight is extracted with a Convolutional Neural Network.

The advantages of camera-based tracking are that they usually require no special equipment apart from a camera and a microscope, as the localization is mainly implemented using software. But the downsides are that the performance of these approaches is heavily influenced by change in illumination, blood and the appearance of the instrument. Furthermore, introducing additional or different instruments requires adaptions. The usage of deep learning further introduces the need for sufficient training data that can be difficult to obtain.

2.3 Structured Light

Structured light imaging is a technique that utilizes specific light patterns to capture the three dimensional shape of a surface. The technique can be used in real-time, offers a high precision and uses no harmful radiation [13].

Like in the camera-based localization, in the structured light-based approaches, a camera and a microscope setup is used to capture the intraocular surface of the eye.

Instead of segmenting the instrument in the captured images, here the projection of structured light is used for the localization.

In [16] structured light is used to construct the surface of the retina relative to a custom optical tracking system. For this reconstruction, two spot lights are moved across the area of interest and the resulting projections are used to reconstruct the surface. Here, the surface of the projection is simplified to be planar. This surface detection is done before the intervention and does therefore not include movements of the eye during the interventions. In [9] the addition of a laser beam detection is proposed to combat the movements.

A similar approach is proposed in [22]. Here, a spot light is directly attached to the instrument. The projection of the spotlight is used to estimate the distance between the instrument and the surface. For the estimation an ellipse is fitted into the projection and the relationship between the distance and the minor axis of the ellipse is utilized.

One advantage of this approach is the direct estimation of the tip-surface distance without introducing further complexity added by reconstructing the surface.

Compared to the camera-based tracking methods, the introduction of the structured light has the advantage of being less influenced by illumination changes and does not

rely on image-based instrument detection. It is also not limited by the availability of training data.

3 Concept

3.1 Overview

Based on the assessment of the state of the art in chapter 2, in this thesis the concept proposed in [22] is extended from a surface to tip estimation to a full localization. Additionally, the usage of more than one spotlight for the reconstruction is evaluated.

3.2 Single Spotlight Localization

The concept for the single spotlight localization is depicted in Figure 3.1. A light fiber is attached to the surgical instrument. A lens concentrates the light of the fiber into a cone shaped light beam. The instrument is inserted into the eye through the sclera, close to the iris. The camera microscope setup is used to capture the retina (a).

The projected light pattern is extracted from the camera image. The contour of the projection is extracted, using post processing and contour detection (b).

Information about the camera setup and the surface are used to reconstruct the three dimensional shape of the contour. An ellipse is fitted into the shape. Based on this fitting and the geometric properties of the light cone, the source position of the light is reconstructed (c).

The reconstructed cone is placed above the projection to obtain the position of the instrument (d).

As the retina closely follows the shape of a sphere, the intraocular surface is simplified to be a sphere.

The theoretical background of the reconstruction is explained in the following chapter.

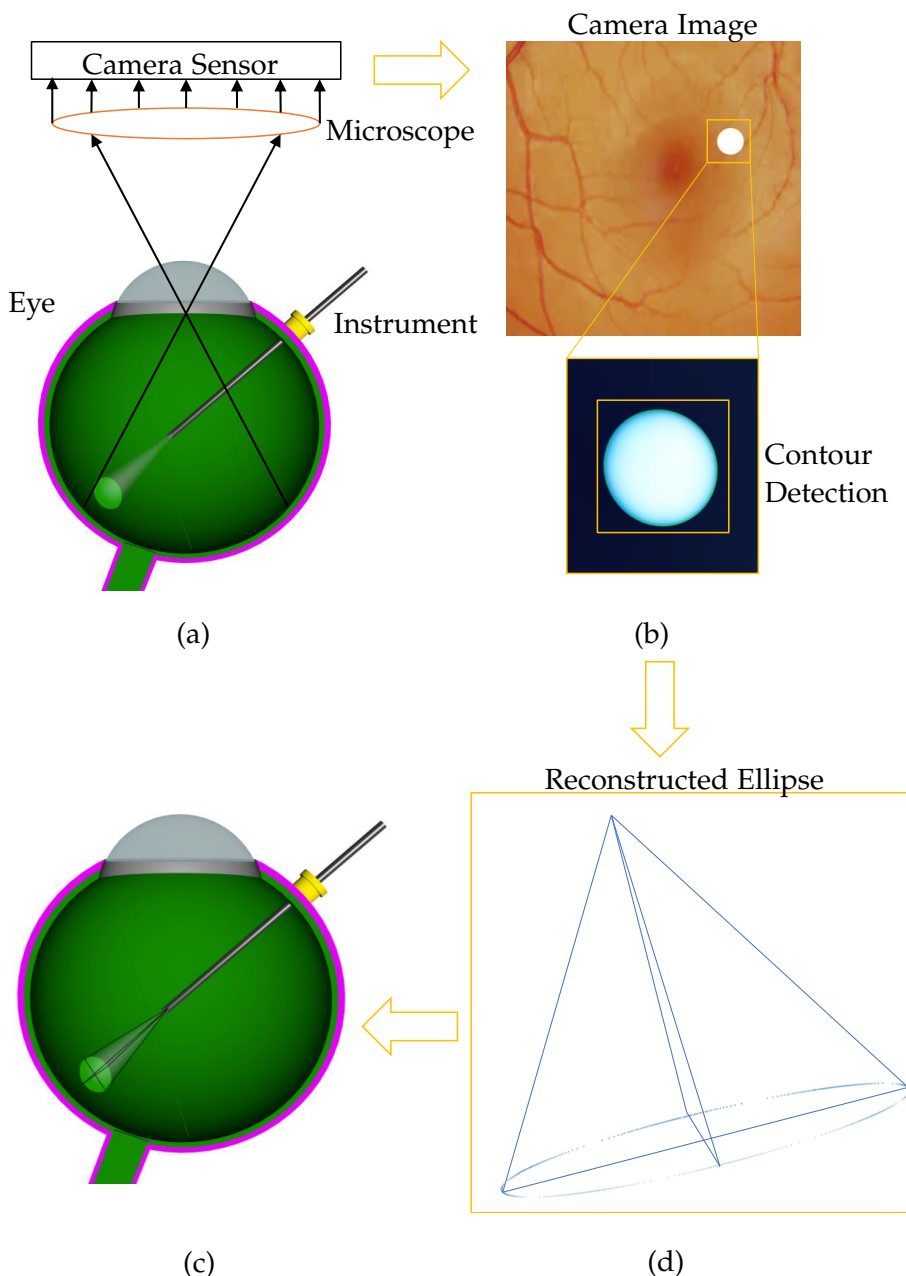


Figure 3.1: Concept for the spotlight-based Localization with a single Spotlight.

3.3 Multiple Spotlight Localization

Additionally, a similar concept with multiple light sources attached to the instrument is evaluated. The concept is depicted in Figure 3.2. The multiple light sources are attached to the instrument with a fixed angle (a). Each of their projections are processed as in the single spotlight version (b). From the resulting positions the median positions is picked as the result (c).

The usage of multiple spotlights has the prospect to increase the accuracy by adding more cues for the localization but comes with a higher construction and calculation effort. As the calculations are independent, they can be performed concurrently, and should not significantly impact the run time in a multi-core system. The usage of a special lens might allow the creation of multiple spotlights based on a single light fiber. It also has to be ensured that the different light beams do not overlap, as otherwise the contour detection will not work.

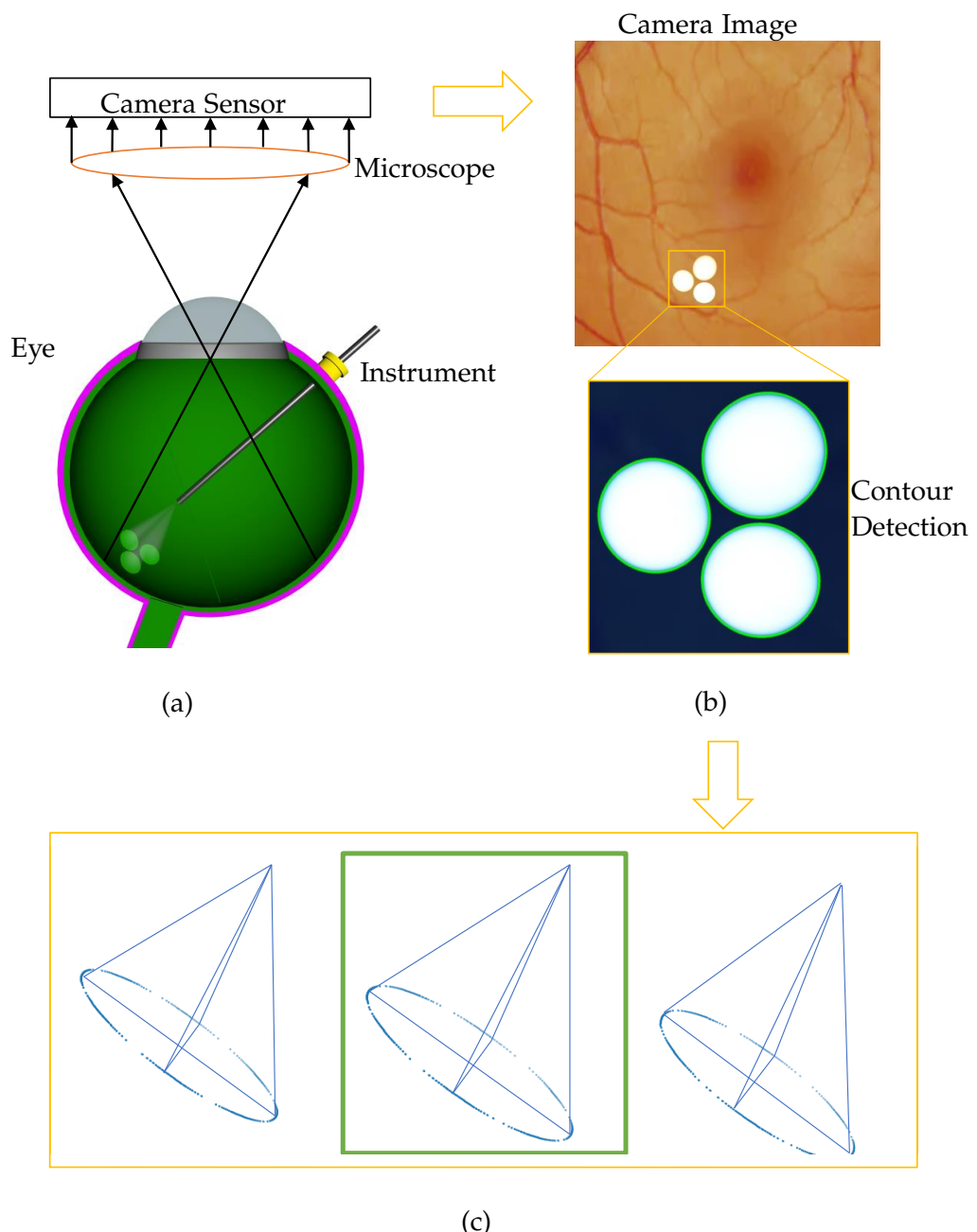


Figure 3.2: Concept for the spotlight-based Localization with multiple Spotlights.

4 Theoretical Background

4.0.1 Pattern Reconstruction

The camera projection of the intraocular surface onto the image plane can be described using the pinhole camera model. As the surface and the camera position and properties are known, they can be used to reconstruct the three dimensional projection from the image. The setting for the reconstruction is depicted in Figure 4.1, where a cross-section through the optical axis is displayed.

For this reconstruction the relationship between the distance of a pixel on the image plane to the pixel representing the center of the sphere (y_1) and the distance between the center of the sphere and the point on the surface represented by this pixel (d) is used. The relationship is given in Equation 4.1, where f is the focal length, r is the radius of the sphere and d_0 is the distance between the focal point and the surface of the sphere.

$$\begin{aligned} a &= 1 + \frac{f^2}{y_1^2} \\ b &= \frac{-2d_0f}{y_1} + \frac{2rf}{y_1} \\ c &= d_0^2 - 2d_0r \\ d &= \frac{-b + \sqrt{b^2 - 4ac}}{2a} \end{aligned} \tag{4.1}$$

Knowing the distance (d) between the point on the optical axis and the point on the surface, we can obtain the corresponding height (h) using Equation 4.2. The height is defined as depicted in Figure 4.1.

$$h = r - \sqrt{r^2 - d^2} \tag{4.2}$$

With the distance we can calculate the expected position (x_r, y_r, z_z) based on the relationship between the distance in x- and y-direction of the point on the image plane (x_p, y_p) to the optical axis. The coordinate system for the image is placed with the origin in the center. The resulting coordinates, with the origin being in the intersection

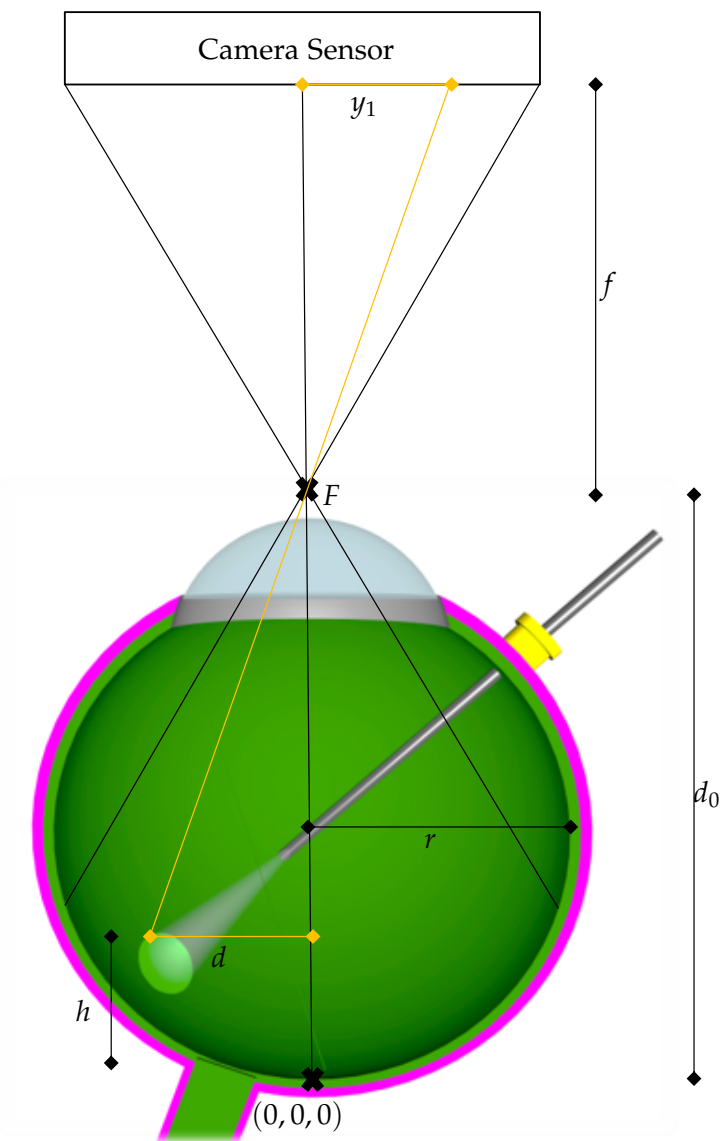


Figure 4.1: Cross-section along the optical Axis. Used for the Reconstruction of the Projection.

between the optical axis and the surface, are given by equations 4.3, 4.4 and 4.5. Here s is the physical size of the camera sensor in mm and p is the resolution of the image sensor.

$$x_r = \begin{cases} \frac{d}{\sqrt{1 + \frac{y_p^2}{x_p^2}}}, & \text{if } x_p \geq 0 \\ \frac{-d}{\sqrt{1 + \frac{y_p^2}{x_p^2}}}, & \text{otherwise} \end{cases} \quad (4.3)$$

$$y_r = \frac{y_p}{x_p} x_r \quad (4.4)$$

$$z_r = \frac{hs}{pd_0} \quad (4.5)$$

This allows to fully reconstruct the three dimensional contour of the intersection based on the shape on captured on the image plane.

4.1 Cone-Sphere Intersection

As the light beam has the shape of a right circular cone, we can see the projected pattern as an intersection between a cone and the surface.

In this case the surface is the back of the eye. The retina closely follows the shape of a sphere [12]. Therefore, we can see the projection of the spotlight as the intersection between a cone and a sphere.

The intersection between a cone and a sphere is a rather complicated three-dimensional curve that does not lie on a two-dimensional plane. The only exception is the special case, where the center of the sphere lies on the axis of the cone, producing a circle-shaped intersection.

Using equations defining a sphere and a cone allows to derive a parametric equation for this curve.

A right circular cone with the vertex in the origin can be defined using Equation 4.6, where β is its opening angle. The angle β is defined as the angle between the axis of the cone and every line from the vertex to a point on its surface. The axis is equal to the z-axis. Only the upper cone is used.

$$z^2 = \frac{x^2 + y^2}{\tan(\beta)^2} \quad (4.6)$$

A sphere can be defined using Equation 4.7, where r is the radius of the sphere and (x_0, y_0, z_0) is the position of the center.

$$(x - x_0)^2 + (y - y_0)^2 + (z - z_0)^2 = r^2 \quad (4.7)$$

Without loss of generality, we can rotate the coordinate system around the axis of the cone, so that the center of the sphere is in the plane defined by the z and x -axis. This allows us to set $y_0 = 0$ and simplify the equation of the intersection. This does not lead to a loss of generality, as the cone is not affected by the rotation. The resulting equation used for the sphere is given in Equation 4.8.

$$(x - x_0)^2 + y^2 + (z - z_0)^2 = r^2 \quad (4.8)$$

We can then obtain an equation for the intersection by combining Equation 4.8 and Equation 4.6. The resulting equation is parametric with x as a parameter. The z -coordinate is given in Equation 4.9 and the y -coordinate in Equation 4.10, where $c = \tan(\beta)$.

$$z = \frac{2z_0 + \sqrt{4z_0^2 - 4(1+c^2)(x_0^2 - r^2 + z_0^2 - 2x_0x)}}{2(1+c^2)} \quad (4.9)$$

$$y = \pm \sqrt{z^2 c^2 - x^2} \quad (4.10)$$

The range of values for x can be calculated using Equation 4.6 and Equation 4.7 and is given in Equation 4.11. The definitions for x_1 and x_2 are given in Equation 4.12 and Equation 4.13.

$$x = [x_1, x_2] \quad (4.11)$$

$$x_1 = \frac{2(x_0 + \frac{z_0}{c}) + \sqrt{(2x_0 + \frac{2z_0}{c})^2 - 4(1 + \frac{1}{c^2}(x_0^2 + z_0^2 - r^2))}}{2(1 + \frac{1}{c^2})} \quad (4.12)$$

$$x_2 = \frac{2(x_0 - \frac{z_0}{c}) - \sqrt{(2x_0 - \frac{2z_0}{c})^2 - 4(1 + \frac{1}{c^2}(x_0^2 + z_0^2 - r^2))}}{2(1 + \frac{1}{c^2})} \quad (4.13)$$

4.2 Cone-Plane Intersection

When inspecting the intersection in three dimensions we can see that the shape is very similar to an ellipse.

This similarity motivates to simplify the real intersection to the shape of an ellipse, as this would significantly reduce the localization effort. Instead of trying to reconstruct the location based on a projection of a three-dimensional curve, we can reconstruct based on the projection of a planar ellipse.

It is also known that the intersection between a cone and a plane has the shape of an ellipse if the angle between the axis of the cone and the plane is higher than the opening angle of the cone.

To show the similarity between the cone-sphere intersection to an ellipse, we construct a plane that intersects the cone and therefore, produces an ellipse shaped intersection.

As we want the cone-plane intersection to be as close to the cone-sphere intersection, we construct a plane through the two points (A and B) on the intersection with the biggest distance in between each other. As we choose $y_0 = 0$ the x-coordinates of these two points are the ends of the range of values of x and can be calculated using Equation 4.12 and Equation 4.13. The corresponding z-coordinates can be calculated using the cone equation as shown in Equation 4.14 and Equation 4.15. The resulting points A and B are given by and Equation 4.16 Equation 4.17.

Figure 4.2 (b) depicts an example for the constructed plane (blue).

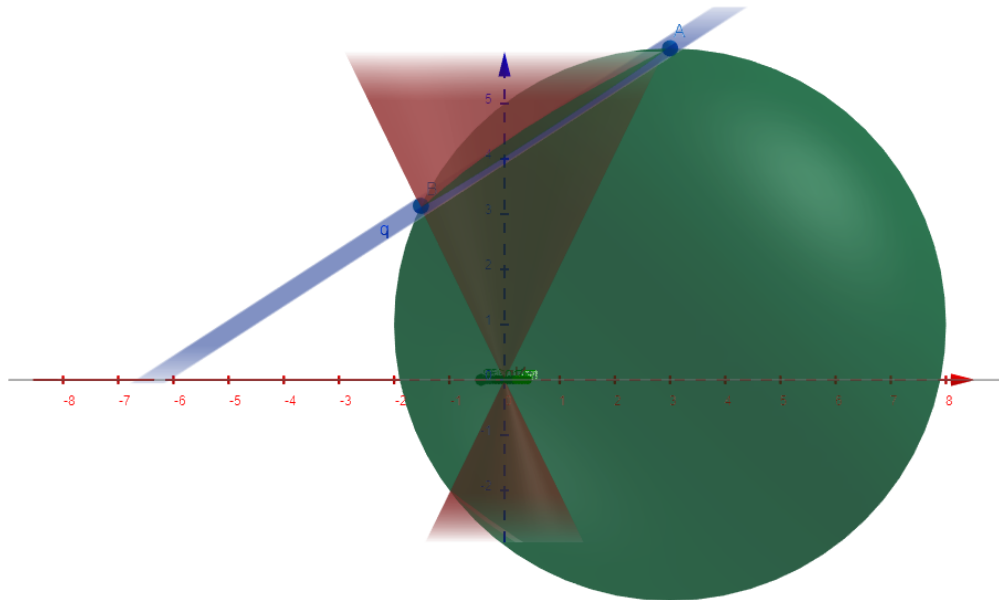


Figure 4.2: Example for the constructed Plane.

$$z_1 = \frac{x_1}{c} \quad (4.14)$$

$$z_2 = \frac{-x_2}{c} \quad (4.15)$$

$$A = \begin{bmatrix} x_1 \\ 0 \\ z_1 \end{bmatrix} \quad (4.16)$$

$$B = \begin{bmatrix} x_2 \\ 0 \\ z_2 \end{bmatrix} \quad (4.17)$$

As the sphere and the cone are symmetric along the zy plane, we construct the plane to share this symmetry by making it parallel to the y-axis.

The resulting plane is defined by Equation 4.18.

$$E : z = \frac{z_1 - z_2}{c(z_1 + z_2)} x + z_1 - \frac{x_1(z_1 - z_2)}{c(z_1 + z_2)} \quad (4.18)$$

This equation can be used in combination with Equation 4.6 to obtain the cone-plane intersection as a parametric (x) equation. The y values are given by Equation 4.19 and the z values by Equation 4.20. Due to the definition of the plane the range of values for x is also given by Equation 4.11.

$$y = \pm \sqrt{\left(\frac{z_1 - z_2}{c(z_1 + z_2)} x - z_1 - \frac{x_1(z_1 - z_2)}{c(z_1 + z_2)} \right)^2 c^2 - x^2} \quad (4.19)$$

$$z = \sqrt{\frac{x^2 + y^2}{c^2}} \quad (4.20)$$

From the definition of the plane, we know that the intersections have the two points A and B in common.

To find the maximum difference between these two intersections we can either use the derivatives of the parametric equations or argue that the intersections have the biggest difference where the two surfaces intersecting the cone have their biggest difference. As the surfaces are a plane and a sphere, we can directly identify the x coordinate of these

two points. The z coordinate for these points can be calculated using the Equation 4.21 and the x coordinate with Equation 4.22.

$$z_h = \cos(\sin^{-1}(\cos(\beta) \frac{x_0}{r}))r + z_0 \quad (4.21)$$

$$x_h = \begin{cases} \sqrt{r^2 - (z_h - z_0)^2} + x_0, & \text{if } x_0 \geq 0 \\ -\sqrt{r^2 - (z_h - z_0)^2} + x_0, & \text{otherwise} \end{cases} \quad (4.22)$$

This allows to directly calculate the maximum difference between the two intersections by using the parametric equations.

For our use case we define an area of interest, mainly limited by the microscope, the camera, and the insertion point of the instrument.

The opening angle of the cone is independent of the location and depends only on the used hardware. Therefore, we calculate the maximum difference for different angles. The resulting maximum differences are given in Table 4.1.

Table 4.1: The maximum Difference between the Intersections.

Opening Angle [°]	5	7	9	11	13	15
Difference [μm]	0.08	0.23	0.49	0.91	1.51	2.34

For our use case these differences are negligible and we can see the projection as an ellipse without introducing a significant error. These differences are calculated based on the values given in Table 4.1.

Table 4.2: Values used for the Calculation of the Maximum Differences.

r	x_0	y_0
12.5	3.7	-6.35

4.3 Camera Projection

As the intersection is projected onto an image plane, we also have to investigate the impact of the difference between the two intersections on the image plane.

Projecting an ellipse in 3D space onto a 2D plane leads to an ellipse except for the special case where the result is a line (90° angle of the ellipse to the plane).

Due to the curvature of the sphere, the angle of the ellipse increases with an increase in x_0 .

We can now use the maximum distance in the y (d_y) and z-direction(d_z) and project it on the image plane to obtain the maximum difference compared to the projection of the ellipse. The camera is positioned at (0,0,0) with the optical axis along the z-axis. The equation for projecting a point (x_s, y_s, z_s) in three dimensions onto the image plane (x_p, y_p) is given in Equation 4.23, where f is the distance of the image plane to the camera.

$$x_p = f \frac{x_s}{z_s} \quad (4.23)$$

$$y_p = f \frac{y_s}{z_s} \quad (4.24)$$

To calculate the distance in y (d_{yp}) and x (d_{xp}) direction on the image plane resulting by the maximum difference between the two intersections, we can use Equation 4.26 and Equation 4.25.

$$d_{yp} = y_s \left(\frac{f}{z_s + d_z} - \frac{f}{z_s} \right) + d_y \frac{f}{z_s + d_z} \quad (4.25)$$

$$d_{xp} = x_s \left(\frac{f}{z_s + d_z} - \frac{f}{z_s} \right) \quad (4.26)$$

As in our case $z_p \gg d_z$, we can simplify the two equations resulting in Equation 4.27 and Equation 4.28.

$$d_{yp} \approx d_y \frac{f}{z_p} \quad (4.27)$$

$$d_{xp} \approx x_p \left(\frac{f}{z_p} - \frac{f}{z_s} \right) = 0 \quad (4.28)$$

This shows that the difference between the two intersections is projected proportionally onto the image plane.

4.4 Ellipse to Cone Reconstruction

For the ellipse fitting, rotations are used to rotate the contour onto the xy plane. After reconstructing the vertex of the cone, the inverse rotations are applied.

The ellipse can be defined using the position of its center, the length of the major (a) and minor axis (b) and its rotation. These are the values used to reconstruct the cone to derive the vertex position.

The size of the minor axis is related to the distance between the vertex of the cone and the plane. The relationship between the major and minor axis depends on the angle between the cone and the plane.

To find the vertex position we use a right triangle as depicted in Figure 4.3. One corner of the triangle is the vertex position and one corner is in the center position. The side s_2 is perpendicular to the xy plane and the side s_1 follows the major axis. The lengths of the side s_1 and s_2 can be calculated using the equations Equation 4.29, Equation 4.30 and Equation 4.31.

$$\alpha = \sin^{-1}(\sqrt{1 - \frac{b^2}{a^2}}) \cos(\beta) \quad (4.29)$$

$$s_1 = a \frac{\sin(2\alpha)}{\sin(2\beta)} \quad (4.30)$$

$$s_2 = a \left(\frac{\cos(2\alpha)}{\sin(2\beta)} + \frac{1}{\tan(2\beta)} \right) \quad (4.31)$$

α is the angle between s_2 and the hypotenuse of the triangle. As the ellipse lies in the xy plane, the corresponding z-coordinate equals the length of s_2 . The x and y-coordinates can be calculated using the rotation of the ellipse and s_1 .

Due to the symmetry of the ellipse two possible positions for the vertex exist. Knowing the rough position of the insertion point allows to narrow it down to one position.

To derive the final result the inverse rotations have to be applied to the vertex position.

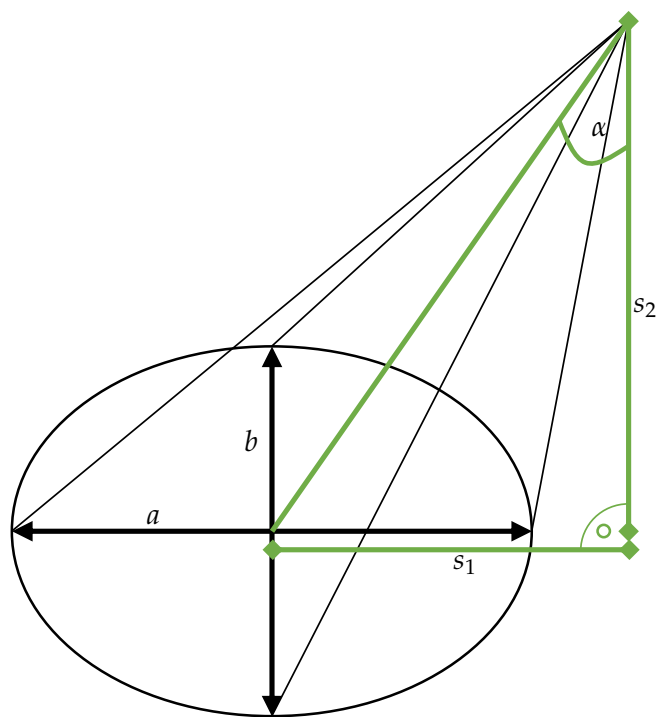


Figure 4.3: Triangle (green) used to derive the Vertex Position based on a given Ellipse.

5 Simulation

5.1 Overview

To test the feasibility of the concept a simulation is used. As light and camera projection should be simulated as realistic as possible, the open source graphic suite Blender 2.8 [3] is used to render the scenes. For the reconstruction of the spotlight position the scripting language Python 3.8 [11] in combination with the computer vision library Open CV [2] is used.

During the simulation the accuracy of the position reconstruction based on the rendered camera image lies in the main focus. The tests and their results are described in chapter 6.

5.2 Blender Setup

The Blender scene contains a spotlight, a half sphere and a camera. To increase the realism, a retina texture is applied to the sphere. The spotlight object has a variable light intensity, opening angle and blurriness factor. It can be moved within the sphere. The rotation of the spotlight is given by a fixed insertion point. The sphere and the camera are static. The camera uses a perspective projection and has a variable focal distance, sensor size and resolution. An image of the setup can be seen in Figure 5.1.

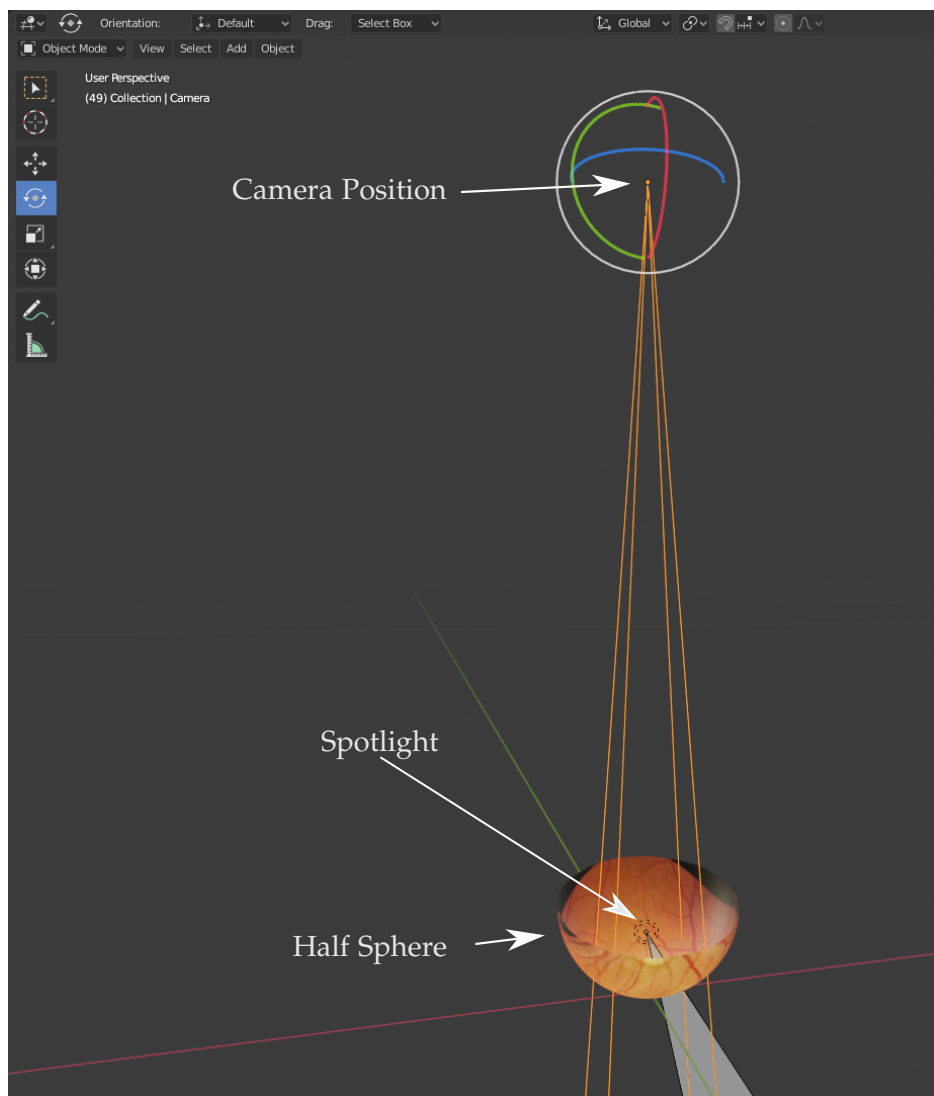


Figure 5.1: Blender Scene used to render the Images.

5.3 Localization Algorithm

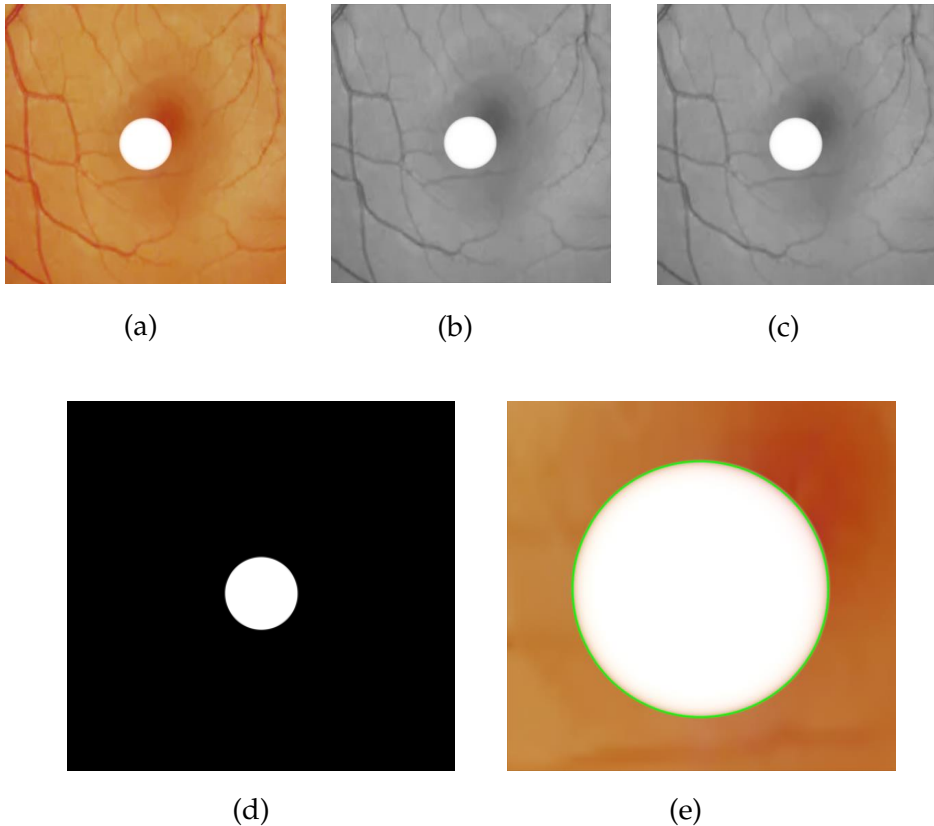


Figure 5.2: Different Steps of the Contour Detection.

The different steps leading up to the detected contour are depicted in Figure 5.2. First the original camera image (a) is converted from RGB to grayscale (b). Then a gaussian and a median filter are applied to reduce the noise (c). The result is converted into a binary image (d) using a threshold obtained with the *Otsu* binarization method. Afterwards, the contour of the projection is detected (e).

The workflow to derive the vertex position based on the camera image is described in algorithm 1.

The contour detection function of the computer vision library OpenCV 2 [2] is used to extract the shape of the projection in the resulting image. As we want as much information about the contour as possible no approximation is used. The detected shape is given in the form of a list of two-dimensional coordinates of the contour.

The equations introduced in chapter 4 are then used to determine the 3D coordinates

Algorithm 1: Localization Algorithm (one Spotlight)

Result: Vertex Positions

load RGB image;

convert from RGB to gray-scale;

apply Median Blur;

apply Gaussian Blur;

convert from gray-scale to binary;

find contours;

for *contour* **in** *contours* **do**

if *contour* **contains more than 5 points** **then**

for *point* **in** *contour* **do**

| calculate represented point on surface;

end

move contour into the origin;

rotate ellipse around z-axis;

rotate ellipse around y-axis;

fit ellipse into the contour;

calculate vertex positions based on ellipse;

rotate vertex around y-axis;

rotate vertex around z-axis;

apply inverse translation;

choose closest point;

return;

end

end

represented by the pixels of the contour on the image. First the euclidean distance of the points on the contour to the center of the image is calculated. This distance is used to calculate the distance of the real point from the optical axis with Equation 4.1. The expected distance in mm is calculated back to pixels using the relationship between the x and the y coordinates of the contour (Equation 4.3 and Equation 4.4). Additionally, a z coordinate is calculated based on Equation 4.2 and Equation 4.5.

The result is a three-dimensional representation of the intersection. To be able to use Equation 4.29, Equation 4.30 and Equation 4.31 to reconstruct the vertex position, rotation and translation are used to move the intersection onto the xy plane. Here the *fitEllipse* function of OpenCV 2 [2] is used to fit an ellipse into the two dimensional representation of the intersection.

The resulting ellipse allows the two possible vertex positions to be calculated using Equation 4.29, Equation 4.30 and Equation 4.31. Finally, the inverse rotation and translation are applied to the vertex positions. In a real-world scenario, the insertion point of the instrument would be known and we can directly choose the correct position based on which position lies on a path between the insertion point and the projection. As we do not have a fixed insertion point in this scenario, we simply choose the point closest to the real position.

5.4 Position Reconstruction with Multiple Spotlights

The reconstruction of the position for the concept with multiple spotlights is based on the reconstruction explained in the previous section. The modified algorithm is given in algorithm 2.

For each projection the two possible vertex positions are derived analog to the single spotlight. To choose the correct positions, all possible combinations including three positions are evaluated based on their spatial difference. The set with the lowest difference is picked. Out of the three resulting positions, the median position is selected as the result.

Algorithm 2: Localization Algorithm (3 Spotlights)

Result: Vertex Positions for multiple Sources

load RGB image;
convert from RGB to gray-scale;
apply Median Blur;
apply Gaussian Blur;
convert from gray-scale to binary;
find contours;
find contours;

for *contour* **in** *contours* **do**

if *contour* **contains more than 5 points** **then**

for *point* **in** *contour* **do**

| calculate represented point on surface;

end

move contour into the origin;
rotate ellipse around z-axis;
rotate ellipse around y-axis;
fit ellipse into the contour;
calculate vertex positions based on ellipse;
rotate vertex around y-axis;
rotate vertex around z-axis;
apply inverse translation;
save resulting positions;

end

end

pick 3 matching positions;
choose median position;

5.5 Calibration

As a countermeasure to errors introduced by the blurriness of the spotlight, the image post processing and imperfect ellipse fittings, a calibration factor for the height can be used.

In a calibration run, the spotlight is positioned in a known distance to the surface. This known distance is divided by the calculated distance to derive a correction factor. This factor can later be applied in the localization.

6 Tests

6.1 Overview

In this chapter tests are performed based on the simulation described in chapter 5. First the ellipse to cone vertex positioning is tested with a plane as a surface. Afterwards the surface is changed to a half sphere and the reconstruction of the projection is added.

The first tests focus on the correctness of the proposed algorithm, while the remaining tests are used to analyze the possibility of using these concepts for complex movements.

6.2 Ellipse-based Vertex Reconstruction

6.2.1 Overview

In this test the accuracy of the ellipse to cone reconstruction based on the camera image using Equation 4.29, Equation 4.30 and Equation 4.31 is evaluated. The surface is changed to be planar. As the goal is to test only the ellipse-based reconstruction, the surface is not textured and the spotlight is designed to produce a sharp projection.

6.2.2 Perpendicular Positioning

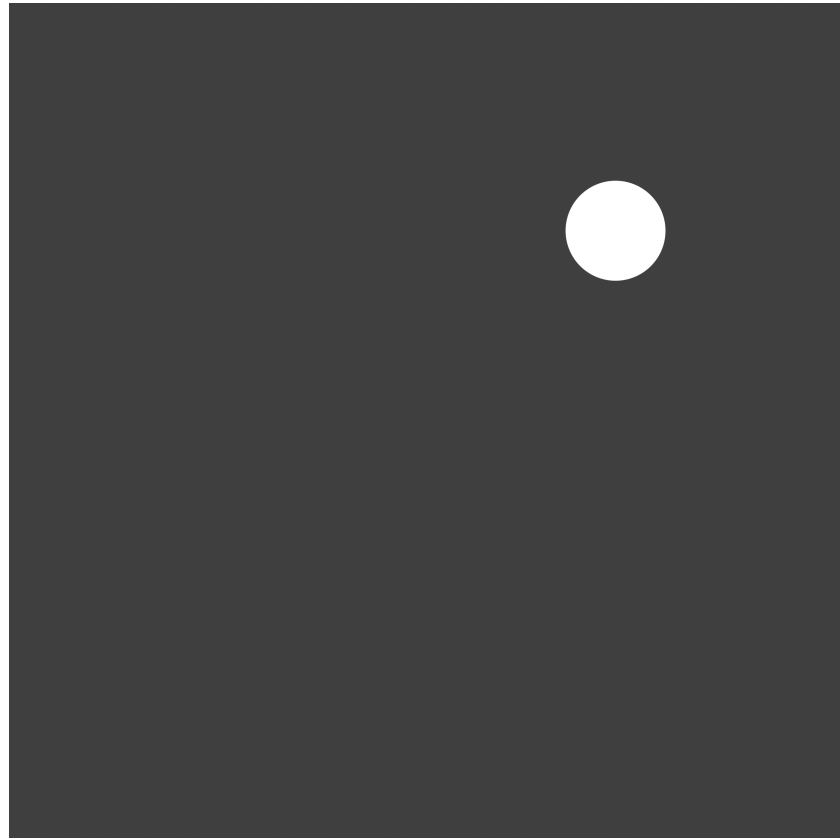


Figure 6.1: Perpendicular Projection on a Plane.

In the first test the spotlight is positioned perpendicular to the surface at the position $(3, 3, 5)$. The resulting camera image is depicted in Figure 6.1. The projection clearly has the shape of a circle. After the post processing the contour is detected in the resulting image. As the surface is planar and parallel to the camera sensor, the contour can be directly used to fit the ellipse. The resulting ellipse is given in table Table 6.1. This ellipse is used to calculate the required values for α , s_1 and s_2 . The results are given in Table 6.2. Due to the perpendicular positioning α should be zero. As this is not the case the value for s_2 is also above zero. The error is caused as the major and minor axis of the ellipse differ by 0.008 pixels. The rotation of the ellipse is responsible for the distribution of the error in y and x direction.

Table 6.1: Ellipse fitted into the Projection onto a Plane (perpendicular).

x-Center [px]	y-Center [px]	Major Axis [px]	Minor Axis [px]	Rotation [°]
3636.825	1363.171	598.410	598.418	83.006

Table 6.2: Values for the Triangle-based Reconstruction (perpendicular).

α [°]	s_1 [px]	s_2 [px]
0.291	9.849	1889.081

Using the rotation of the ellipse and the values for s_1 and s_2 we can obtain the two positions. After using the camera settings to calculate the positions in mm with the origin located in the center, the resulting positions are $(2.974, 2.997, 4.987)$ and $(3.026, 3.003, 4.987)$. We can see that the error of 0.291° for α does not cause a significant error.

6.2.3 Angled Positioning

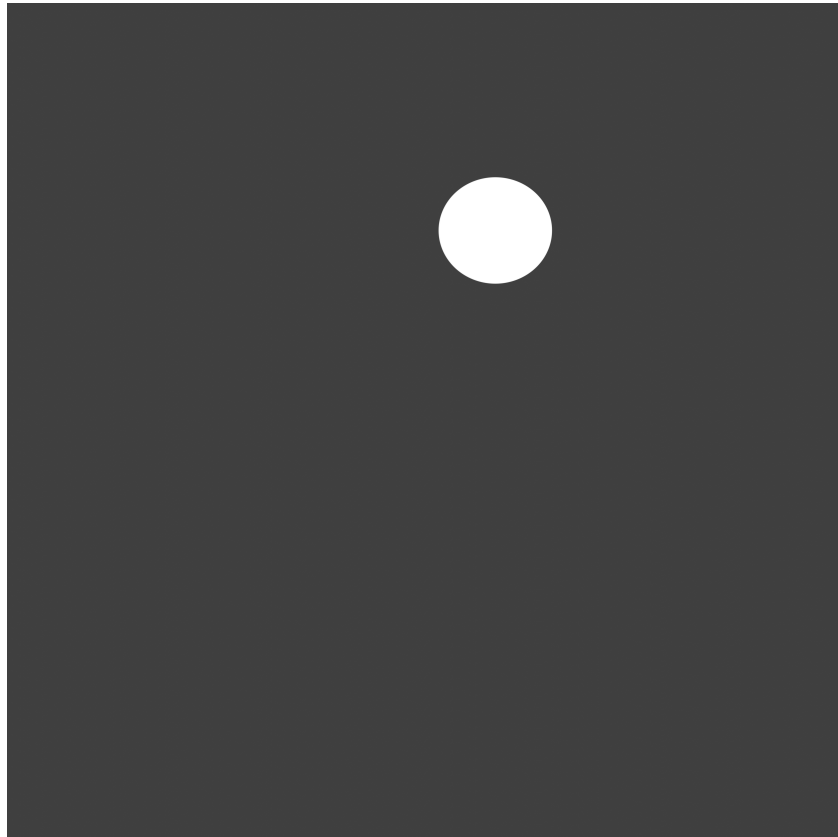


Figure 6.2: Angled Projection on a Plane.

Now the spotlight is placed at the same location, but rotated around its y-axis by 20° . The camera image can be seen in Figure 6.2. Here the projection is not shaped like a circle anymore. The fitted ellipse is given in Table 6.3 and the calculated values for α , x and h in Table 6.4. We can directly see that the angle α differs only by 0.010° from the used rotation. The rotation of the ellipse is also correctly detected with 90° . Calculating the two possible positions as in the previous example yields the two results $(-0.738, 3.000, 4.985)$ and $(2.996, 3.000, 4.985)$.

Table 6.3: Ellipse fitted into the Projection onto a Plane (angled).

x-Center [px]	y-Center [px]	Major Axis [px]	Minor Axis [px]	Rotation [$^\circ$]
2927.043	1363.152	637.629	679.726	90.000

Table 6.4: Values for the Triangle-based Reconstruction (angled).

α [°]	s_1 [px]	s_2 [px]
20.010	707.246	1888.253

6.3 Projection and Vertex Reconstruction

Here, the surface is changed from a plane back to a half sphere. This adds the reconstruction of the projection based on the surface to the test.

6.3.1 Perpendicular Positioning

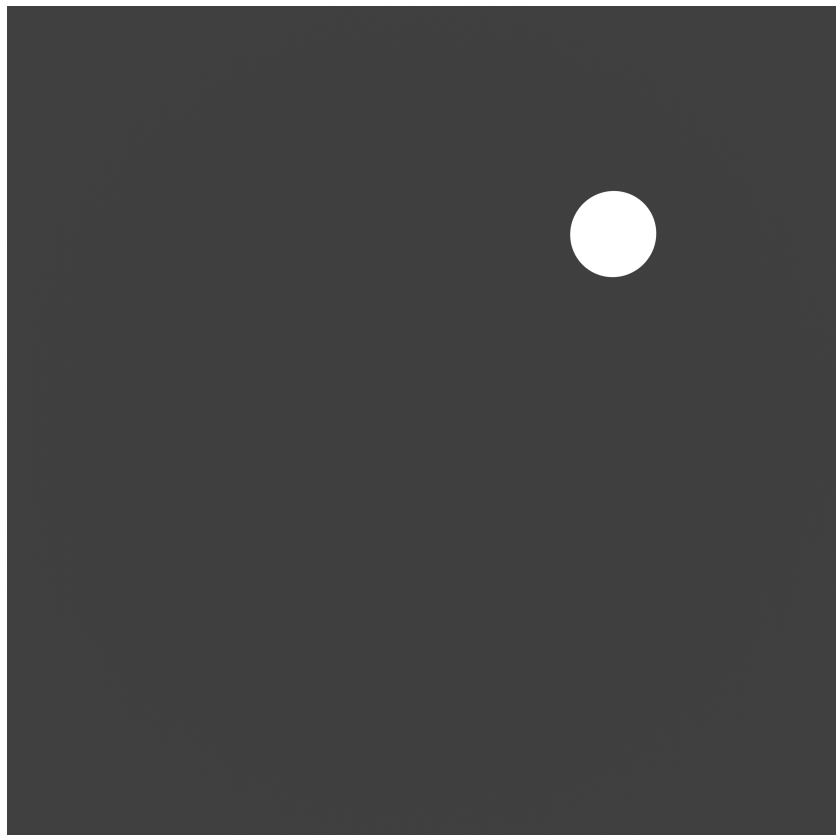


Figure 6.3: Projection on a Sphere.

The spotlight is again positioned parallel to the z-axis at location (3,3,5). The resulting camera image is displayed in Figure 6.3 . Unlike in the previous test, we cannot directly use the contour to fit the ellipse, but have to reconstruct the projection first. Equation 4.3 is used to calculate the real projection based on the surface.

This contour is then moved into the origin and rotated by the angle of the sphere (19.519°) at the center position of the reconstructed position. To simplify the calculations, the rotation is split into one rotation around the z-axis (45.025°) to position the center of the projection on the x-axis and a second rotation around the y-axis to compensate the angle of the surface of the sphere. The resulting contour is used to fit the ellipse. The resulting ellipse is given in Table 6.5. Again the values for α , x and h are calculated and given in Table 6.5. Now the two vertex positions can be calculated.

Table 6.5: Ellipse fitted into the reconstructed Projection onto a Sphere.

x-Center [px]	y-Center [px]	Major Axis [px]	Minor Axis [px]	Rotation [°]
3624.604	1372.510	508.126	540.028	89.993

Table 6.6: Values for the Triangle-based Reconstruction (Sphere).

α [°]	s_1 [px]	s_2 [px]
19.539	550.810	1509.331

The inverse rotations and translations have to be applied to the resulting vertex positions. The resulting positions are then given by (1.060,1.063,4.020) and (2.997,3.002,4.991), where the second position has a distance of 0.009 mm to the real position.

6.4 Linear Movement

6.4.1 Overview

In this test the instrument is moved along a path defined by 4 points (P1-P4) given in Table 6.7. The angle of the instrument is given by the position of the insertion point placed at (0,6,20), which is also the center of motion. The path is visualized in Figure 6.4. The arrows are used to indicate the rotation of the instrument. During the movement the localization algorithm is used 100 times. The dots resemble the positions where the localization is executed.

6 Tests

Table 6.7: Coordinates of the Points that define the Path for the first Test (Square).

	x	y	z
P1	-2.5	-2.5	3
P2	2.5	-2.5	4
P3	2.5	2.5	5
P4	-2.5	2.5	6

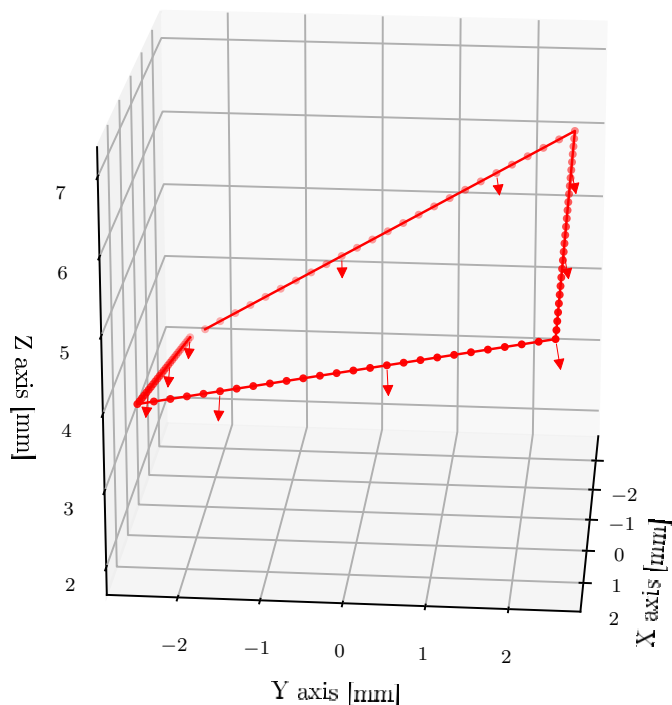


Figure 6.4: Path of the Spotlight used during the first Test (Helix).

The properties of the simulation, as introduced in the previous chapters, are given in Table 6.8.

Table 6.8: Properties of the Camera in the Blender Simulation.

Resolution (p)	Sensor Size (s)	Focal Length (f)	Angle (β)
5000 pixels	3.6 cm	30 cm	9°

The test is performed with one spotlight and three spotlights.

6.4.2 Result

To analyze the performance of the localization algorithm, the resulting positions are compared to the original positions. The reconstructed positions (dots) on top of the real trajectory (line) are displayed in Figure 6.5 and Figure 6.6.

The reconstructed positions closely follow the real path. The euclidean distance between the real and the reconstructed positions in mm (y-axis) for both versions is plotted in Figure 6.7 for each step (x-axis).

Here, we can see that usage of three spotlights is able to slightly decrease the positioning error in this test. The improvement is also quite visible when looking at the average and maximum euclidean error as given in Table 6.9.

Table 6.9: Positioning Error (Euclidean Distance) for the first Test.

	Single Spotlight	3 Spotlights
Average Error (Square) [mm]	0.026	0.023
Maximum Error (Square) [mm]	0.100	0.074

The error for each direction (x,y,z) is depicted in Figure 6.8 and shows no strong bias towards a specific direction, but we can see that the y-direction seems to be calculated with a slightly better accuracy.

Finally, the rotation of the instrument is modelled using rotations in y and z direction. The error of the prediction is depicted in Figure 6.9 and the average and maximum error is given in Table 6.10. Similar to the positioning error, the rotational error is improved using the version with multiple spotlights.

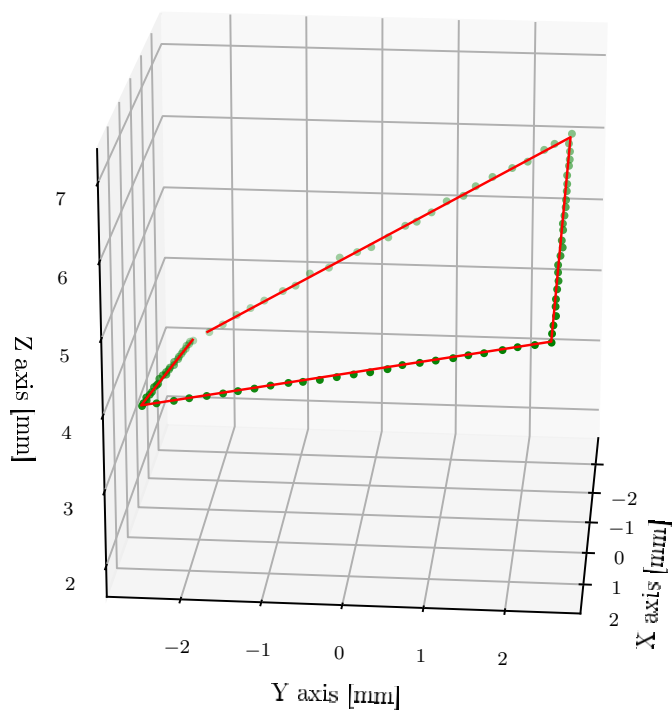


Figure 6.5: Reconstructed Positions (green) using one Spotlight for the first Test (Square).

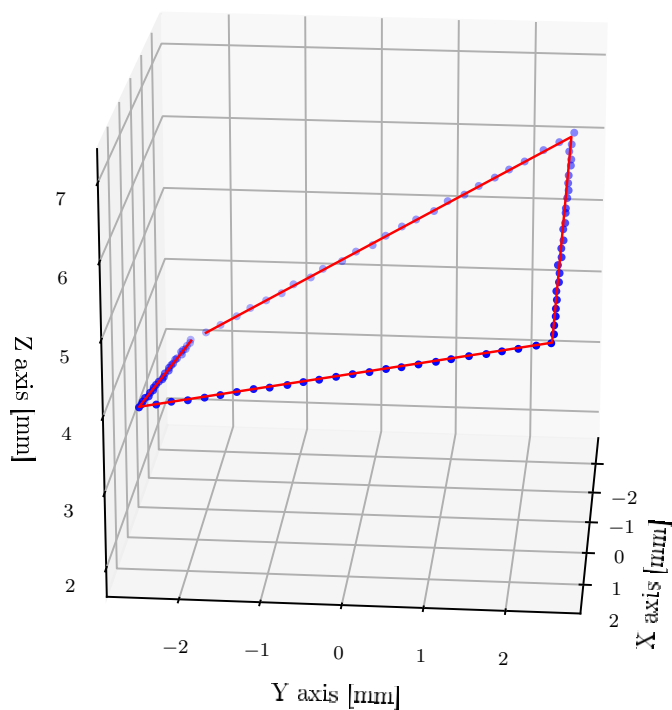


Figure 6.6: Reconstructed Positions (blue) using three Spotlights for the first Test (Square).

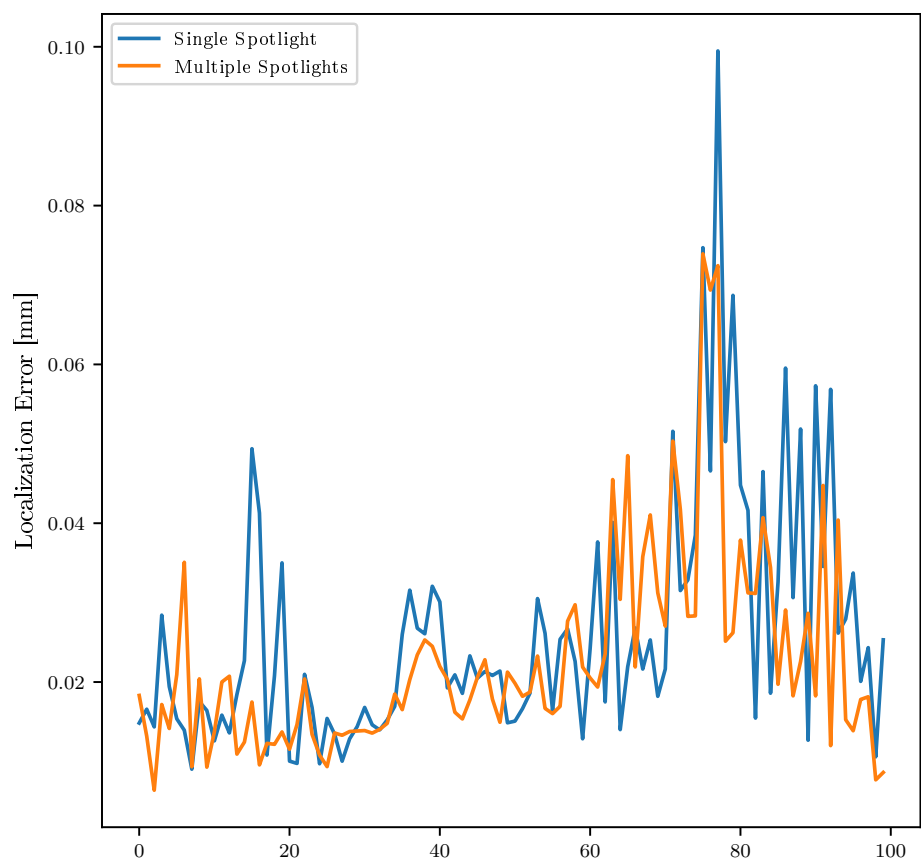


Figure 6.7: Euclidean Distance between the reconstructed and real Positions for the first Test (Square).

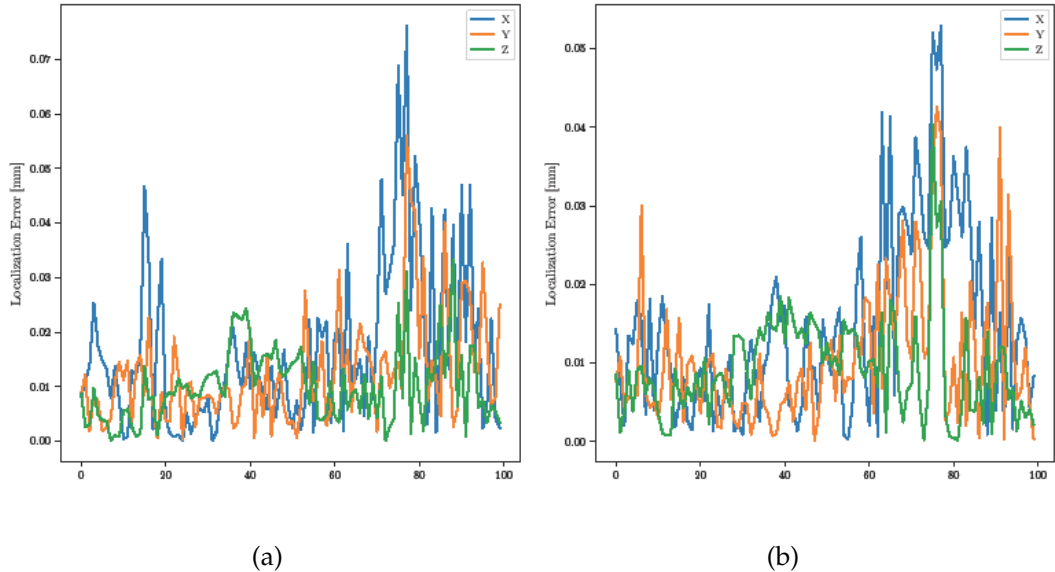


Figure 6.8: Euclidean Distance between the reconstructed and real Positions separated into the x,y,z Direction. (a) Single Spotlight, (b) Three Spotlights

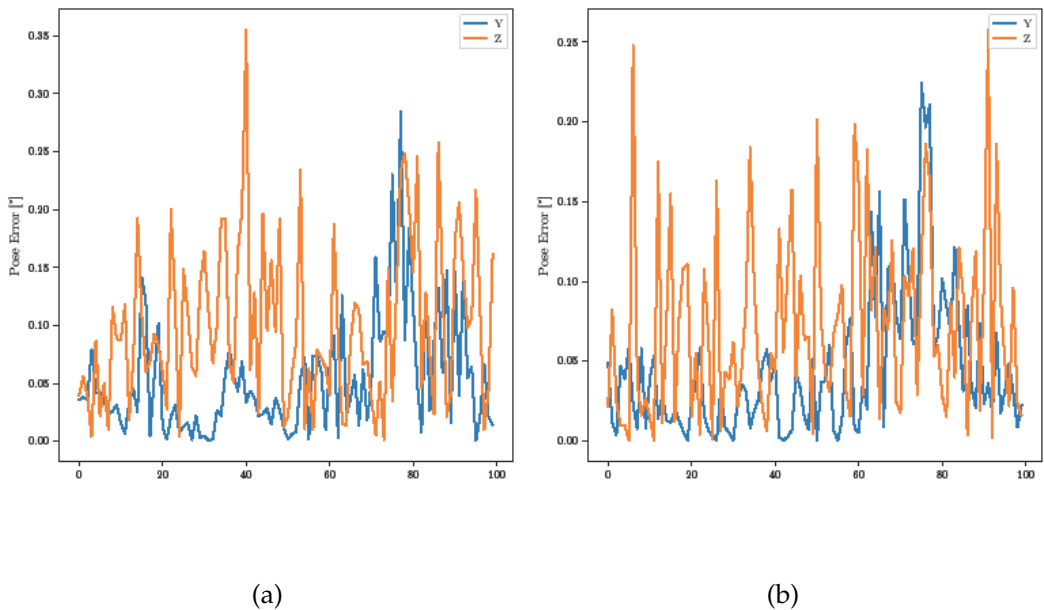


Figure 6.9: Rotational Error of the Prediction. (a) Single Spotlight, (b) Three Spotlights

Table 6.10: Rotational Error for the first Test.

	y-axis	z-axis
Average Error (single spotlight)	0.053°	0.100°
Maximum Error (single spotlight)	0.285°	0.355°
Average Error (three spotlights)	0.044°	0.072°
Maximum Error (three spotlights)	0.224°	0.258°

6.5 Helix Movement

For the second test, the path is chosen to resemble the structure of a helix. The rotation of the instrument is again defined by the insertion point (0, 6, 20). The path is depicted in Figure 6.10, with the arrows again indicating the rotation and the points resemble the positions where the localization is tested. The settings of the camera and environment are kept equal to the previous test.

6.5.1 Result

The resulting positions are again plotted on top of the real path. In Figure 6.11 the result using a single spotlight can be seen and in Figure 6.12 the result for the version with multiple spotlights. The positions again clearly resemble the correct path, with slight deviations.

The difference measured as the euclidean distance along the tested positions is given in Figure 6.13. We can again see that the version with multiple spotlights improves the error slightly. The average and maximum errors are given in Table 6.11.

Table 6.11: Positioning Error (Euclidean Distance) for the second Test (Helix).

	Single Spotlight	3 Spotlights
Average Error (Helix) [mm]	0.031	0.026
Maximum Error (Helix) [mm]	0.133	0.080

In Figure 6.14 and Figure 6.15 the error separated in x,y and z direction, as well as the rotational error are given. The summation is given in Table 6.12

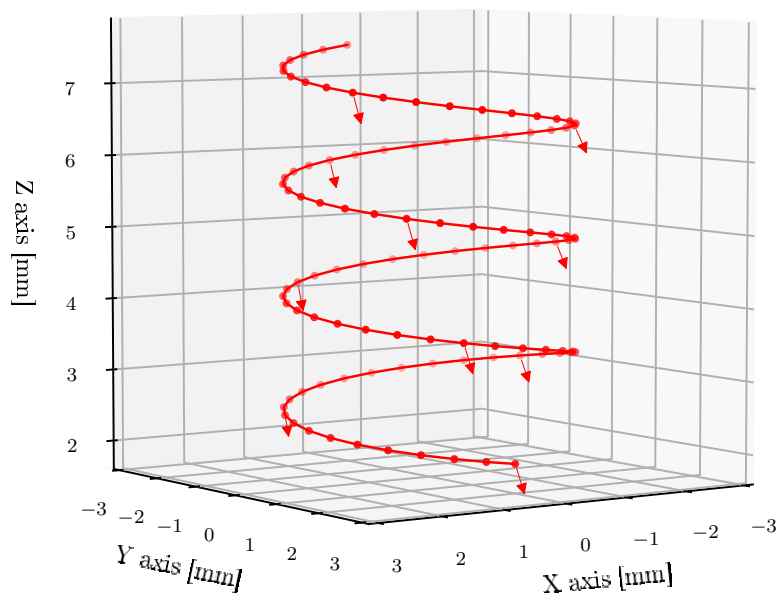


Figure 6.10: Path of the Spotlight used during the second Test (Square).

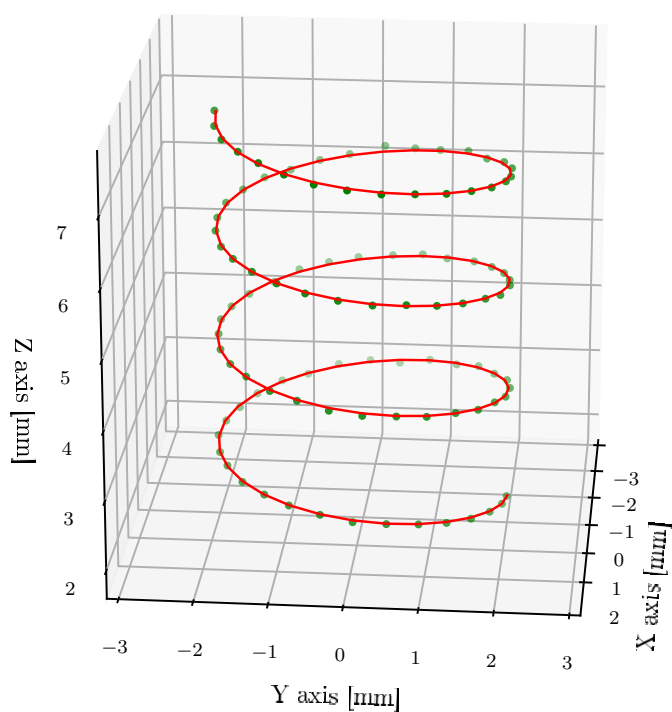


Figure 6.11: Reconstructed Positions (green) using one Spotlight for the second Test (Helix).

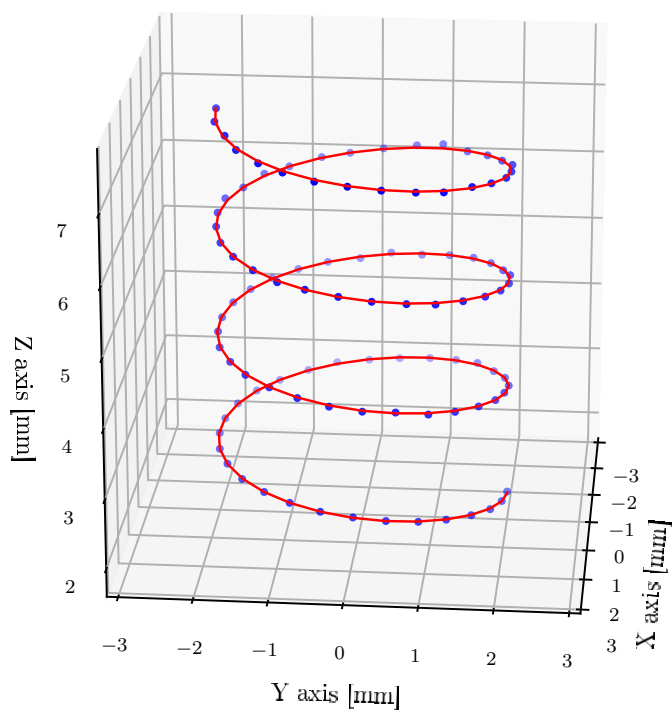


Figure 6.12: Reconstructed Positions (blue) using three Spotlights for the second Test (Helix).

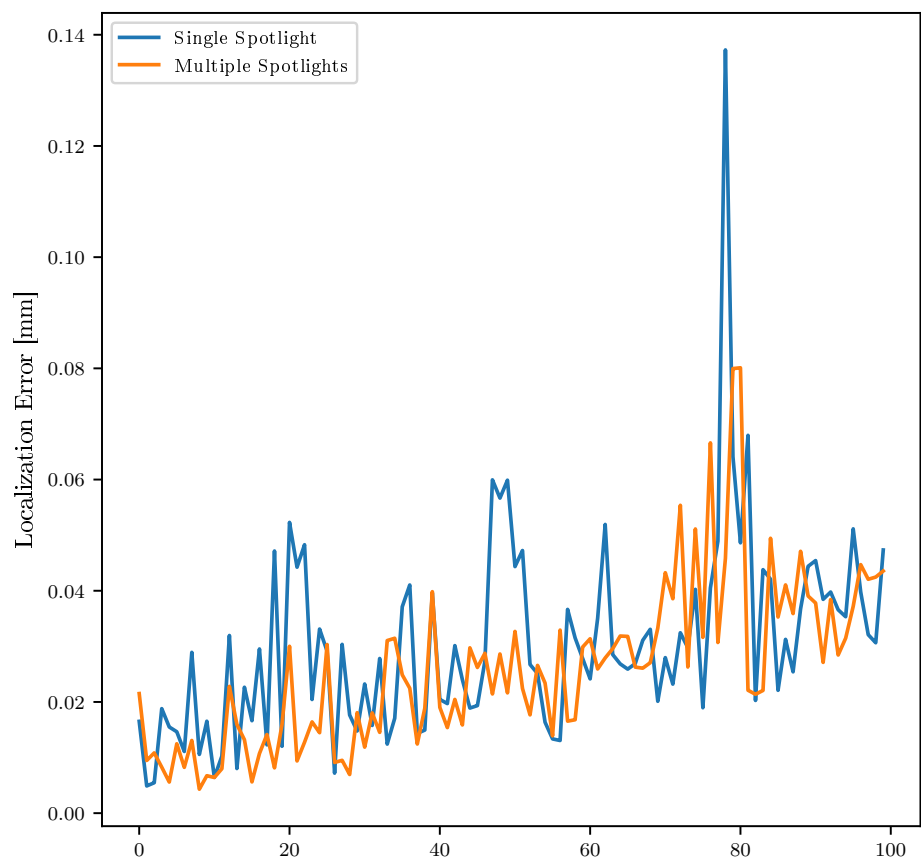


Figure 6.13: Euclidean Distance between the reconstructed and reference Positions.

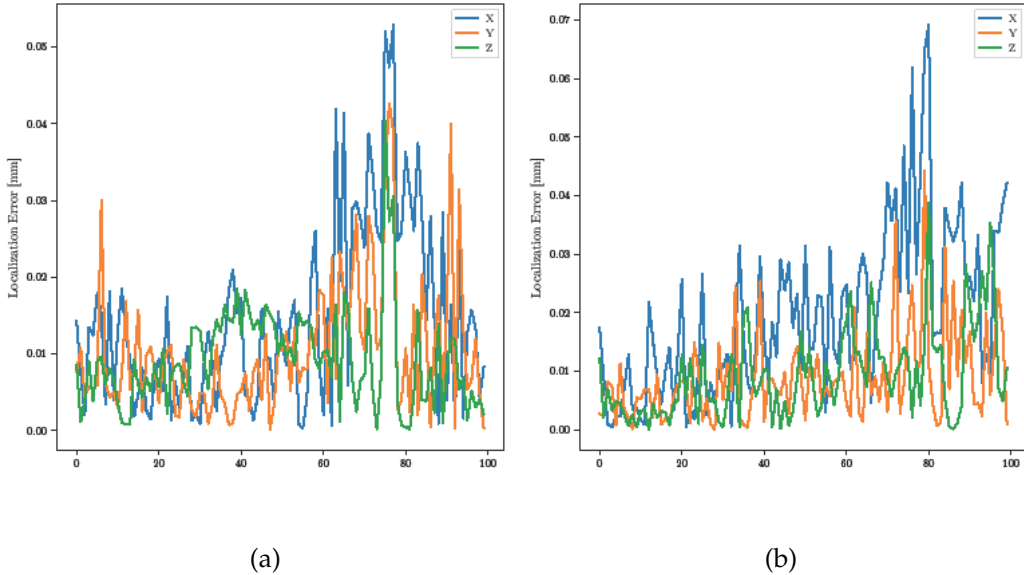


Figure 6.14: Euclidean Distance between the reconstructed and reference Positions separated into the x,y and z Direction. (a) Single Spotlight, (b) Three Spotlights

Table 6.12: Rotational Error for the second Test.

	y-axis	z-axis
Average Error (single spotlight)	0.070°	0.089°
Maximum Error (single spotlight)	0.436°	0.230°
Average Error (three spotlights)	0.058°	0.077°
Maximum Error (three spotlights)	0.263°	0.036°

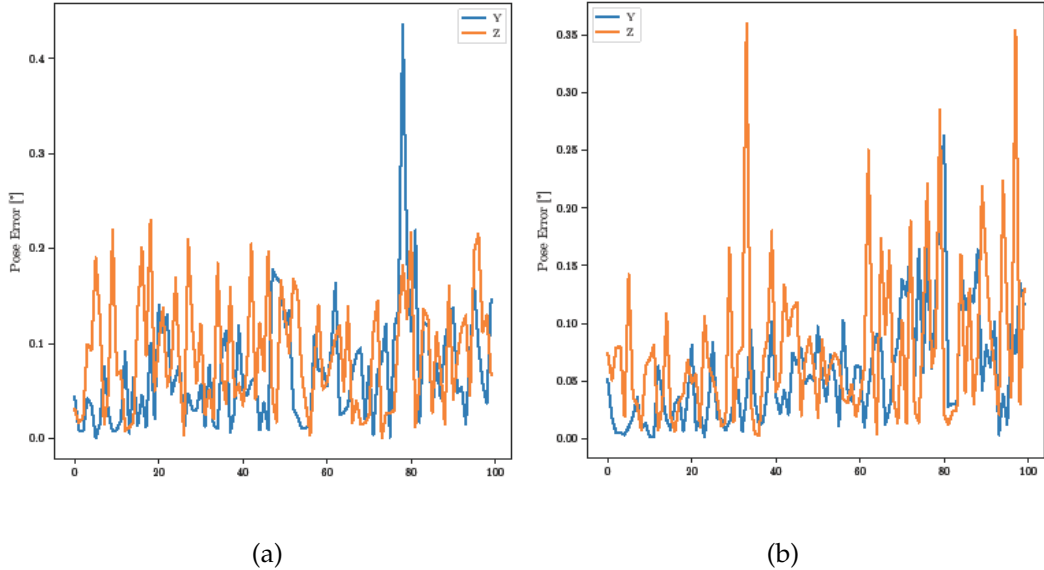


Figure 6.15: Rotational Error of the Prediction. (a) Single Spotlight, (b) Three Spotlights

6.6 Light Intensity

The results for the previous two tests are conducted using a fixed intensity for the spotlights. In a realistic scenario the projection is heavily influenced by environment lighting and the intensity of the utilized spotlights.

In this section the previous two tests are conducted using different intensities and the results are compared.

The intensity is controlled by using a different values for the power in Blender, which equals to the light emitted by the source. The results in the previous tests were obtained using a power value of 1 Watt.

The appearance changes of the spotlight projection on the camera image can be seen in Figure 6.16. The intensity is tested for the values 0.01 Watt (a), 0.1 Watt (b), 0.25 Watt (c), 0.5 Watt (d), 1 Watt (e), 1.5 Watt (f) and 2 Watt (g). For these projections the spotlight is placed at the position (0,0,8) perpendicular to the surface.

Between the first 4 images, a clear difference in the brightness and the blurriness of the projection is visible. In the remaining images only a slight difference in the blurriness can be seen.

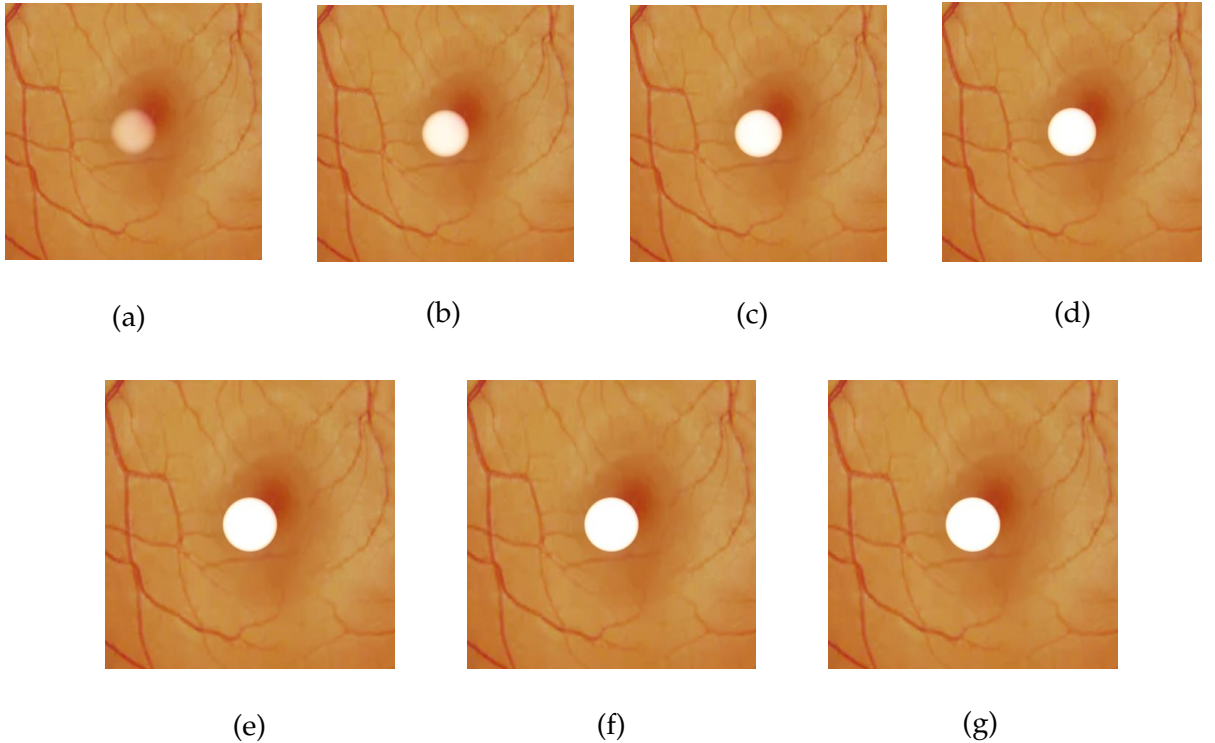


Figure 6.16: Projections using different intensities for the Spotlight.

6.6.1 Results

The average localization errors (euclidean distance) obtained in this test are given in Table 6.13 and Table 6.14 and are visualized in Figure 6.17. The curve show a clear correlation between the average error and the intensity of the light, even though the overall change is quite small.

In Table 6.13 and Table 6.14 the average and maximum positioning error (euclidean distance) in mm is given for the first test. We can directly see a correlation between the intensities and the errors. A lower intensity leads to a bigger error and vice versa. We can also see that the error using the last few intensities is barely influenced. Additionally the maximum error shows a much higher variance compared to the average error.

The version with multiple spotlights does not only consistently result in a smaller error, but also has a much better result for the lowest intensity (0.158 mm and 0.263 mm).

In Table 6.15 and Table 6.16 the average and maximum positioning error (euclidean distance) in mm is given for the second test. The results are similar to the first test, but

Table 6.13: Positing Error (euclidean) for different intensities in the first Test using a single Spotlight.

Intensity [Watt]	Average Error [mm]	Maximum Error [mm]
0.01	0.093	0.263
0.1	0.040	0.153
0.25	0.033	0.121
0.5	0.029	0.107
1	0.026	0.100
1.5	0.025	0.097
2	0.025	0.088

Table 6.14: Positing Error (euclidean) for different intensities in the first Test using three Spotlights.

Intensity [Watt]	Average Error [mm]	Maximum Error [mm]
0.01	0.086	0.158
0.1	0.037	0.083
0.25	0.029	0.075
0.5	0.025	0.073
1	0.023	0.074
1.5	0.021	0.073
2	0.020	0.072

higher. Again, a clear correlation between the errors and the intensities can be seen, especially for the first four samples. For the intensity of 0.01 Watt, the maximum error is significantly higher for both the version with a single spotlight (0.603 mm) and the version with multiple spotlights (0.300 mm).

Table 6.15: Positing Error (euclidean) for different intensities in the second Test using a single Spotlight.

Intensity [Watt]	Average Error [mm]	Maximum Error [mm]
0.01	0.126	0.603
0.1	0.051	0.242
0.25	0.039	0.167
0.5	0.034	0.152
1	0.031	0.133
1.5	0.029	0.129
2	0.028	0.122

The average error of both tests with different intensities is plotted in Figure 6.17. In the plot again the clear correlation between the intensity and the error is visible. We can also see that the average error is in an acceptable range below 0.1 mm for the intensity 0.1 Watt and above. As expected the version with multiple spotlights outperforms the version with a single spotlight.

The maximum error for both tests is plotted in Figure 6.18. Compared to the average error, a much higher variance is visible. Similar to the average error, the maximum error does not improve significantly above the intensity of 0.5 Watt. Due to the high maximum error, the intensities below 0.25 Watt are not adequate for this simulation.

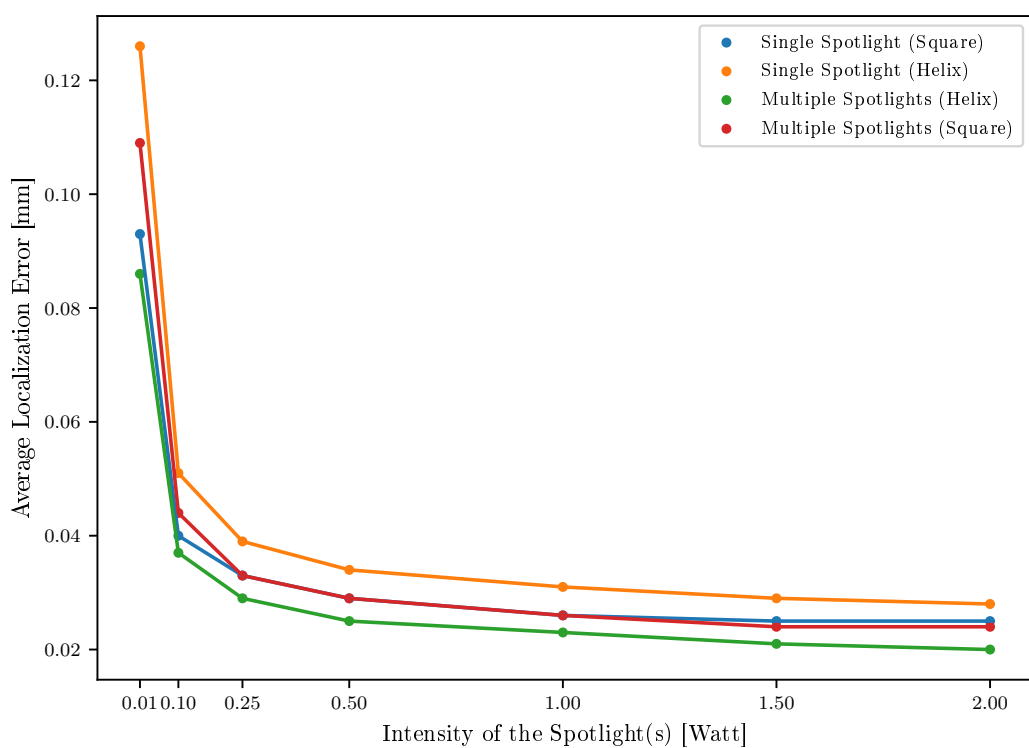


Figure 6.17: Average Error of the Prediction for different Intensities.

Table 6.16: Positing Error (euclidean) for different intensities in the second Test using three Spotlights.

Intensity [Watt]	Average Error [mm]	Maximum Error [mm]
0.01	0.109	0.300
0.1	0.044	0.092
0.25	0.033	0.078
0.5	0.029	0.081
1	0.026	0.080
1.5	0.024	0.083
2	0.024	0.086

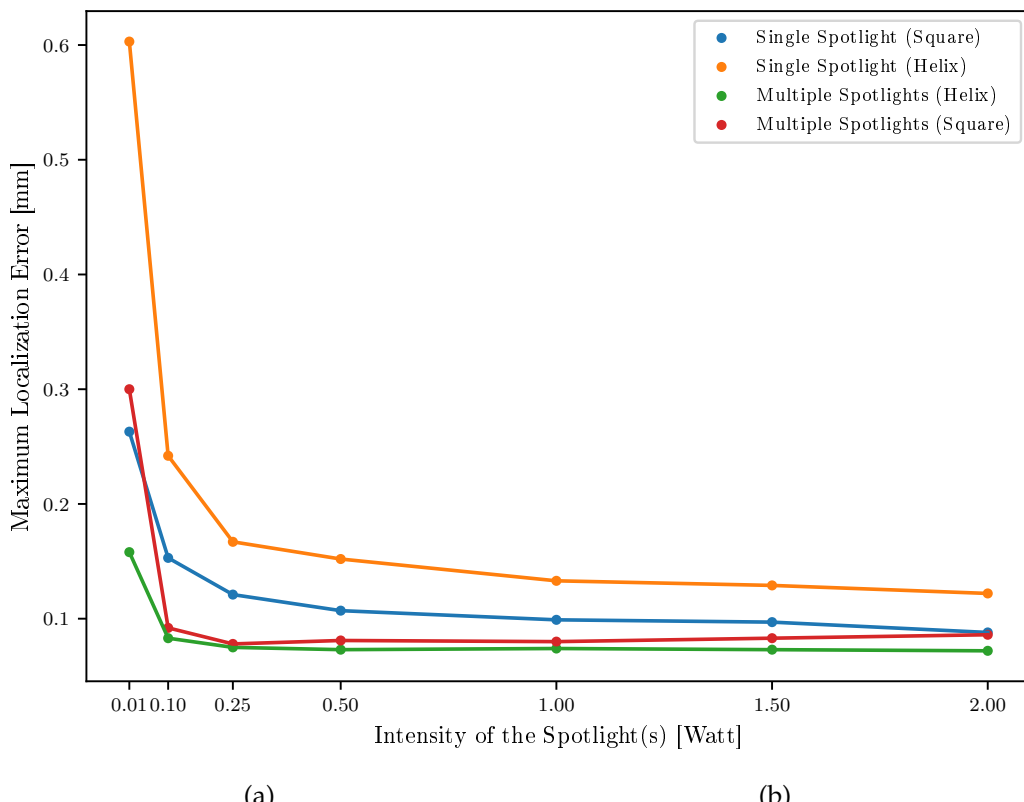


Figure 6.18: Maximum Error of the Prediction for different Intensities.

6.7 Deformed Surface

The impact of small deformations on the surface is tested by adding 15 bumps with a radius of around 0.25 mm and a deviation in height from the sphere surface of 0.1 mm. The bumps are placed in a 3x5 grid formation across the area of interest.

6.7.1 Results

The bumps do not affect the localization as long as they are either completely inside or outside the projection. In the case where a bump lies on the edge of the projection, the resulting contour does not have the shape of an ellipse. After the reconstruction of the shape based on the surface, the fitted ellipse might differ depending on the impact on the contour. Here, an impact on the properties of the ellipse (major axis, minor axis, rotation, or center position) directly leads to an error for the vertex reconstruction. An example for the caused changes in the projection is depicted in Figure 6.19. Here, the top and the left projection are miss shaped due to the bump.

For this test the second movement (Helix) is performed. The resulting euclidean errors are given in Table 6.17. The average errors are very close the the test without the deformation. This hints that the case where the bump directly affects the ellipse fitting occurred rarely. The maximum error of the version with a single spotlight is significantly higher with a value of 0.210 mm compared to 0.133 mm. The maximum error of the version with multiple spotlights is equal to the maximum error during the test without the deformations. This again demonstrates the increased robustness of the version with three spotlights.

Table 6.17: Positioning Error (Euclidean Distance) for the second Test (Helix) with a deformed Surface.

	Single Spotlight	3 Spotlights
Average Error (Helix) [mm]	0.035	0.027
Maximum Error (Helix) [mm]	0.210	0.080



Figure 6.19: Example for the Impact of the Deformation on the Projection.

6.8 Curvature

For the calculation of the reconstructed projection based on the camera image the radius of the sphere is needed. With this test the impact of using a wrong radius for the reconstruction is tested. The sphere is adapted to have a radius of 1.35 mm while using a radius of 1.25 mm for the calculations. The second movement (Helix) is performed.

6.8.1 Results

Due to the different curvature, the impact of the wrong radius increases with an increasing distance from the center. This leads to a high localization error. The resulting average and maximum errors are given in Table 6.18. Both versions produce high average and an unacceptable maximum error. This shows that it is important to choose a very similar radius for calculations.

Table 6.18: Positioning Error (Euclidean Distance) for the second Test (Helix) with a wrong Radius.

	Single Spotlight	3 Spotlights
Average Error (Helix) [mm]	0.151	0.144
Maximum Error (Helix) [mm]	0.566	0.566

6.9 Calibration

In the conducted tests the addition of a calibration as introduced in the previous chapter did not lead to an improvement in the accuracy and is thus not used for the presented results.

7 Conclusion

7.0.1 Concepts

In this thesis the concept for the surface to tip estimation using a structured light as presented in [22] is extended to a full three-dimensional localization within the eye, including the rotation of the instrument. In the previous work an ellipse is fitted into the projection of the spotlight and a previously obtained relationship between the tip-to-surface distance is used. The extensions required for this work include reconstructing the projection based on the surface, fitting an ellipse into the reconstructed position and using geometrical properties of the ellipse and the light cone to estimate the position of the instrument.

To simplify the reconstruction, the projection pattern is assumed to be a planar ellipse instead of a three-dimensional curve. This allows the projection to be seen as a plane-cone intersection.

Due to the simplicity of the algorithm a localization in real-time should be easily achievable.

With the prospect of an increased accuracy and higher stability, a concept with multiple spotlights attached to the instrument is also analyzed. The spotlights are angled to ensure that their projections do not overlap in the desired working area. Each of the resulting projections is used independently to derive a possible vertex position. From the three resulting positions, the median position is chosen as the result. Here, more sophisticated approaches might further improve the results.

7.0.2 Simulation

To analyze the viability of the proposed concepts, a high fidelity simulation is created. The scene is modeled using the graphic suite Blender 2.8. To increase the realism a texture is added to the surface to resemble the retina, and blur is introduced for the spotlight. The scripting language Python in combination with the Computer Vision Library OpenCV 2 [2] is used for the post processing of the image and the calculations required for the algorithm.

7.0.3 Results

During the tests the version with a single spotlight is able to localize the instrument during a complex movement with an average positioning error of less than 0.04 mm and a maximum error below 0.15 mm.

With three spotlights the average error is improved to less than 0.03 mm, while the maximum error is brought down below 0.010 mm. For the test 200 unique positions for the instrument were tested.

The influence of the intensity of the spotlight is additionally tested by performing the movement with different levels of intensities, varying between 0.01 Watt and 2 Watt. The error does not change significantly above 0.5 Watt. Below 0.25 Watt the intensity becomes too low, leading to an unacceptable maximum error of up to 0.603 mm.

To test how the concept works with a deformed surface, 15 small bumps with a height of around 0.1 mm are added to the sphere. Both versions are still able to achieve a similar average error. The maximum error for the single spotlight is significantly higher with a value of 0.210 mm, compared to 0.080 mm for the version with three spotlights.

Overall, the version with multiple spotlights is able to significantly improve the results, especially under bad conditions such as a deformed surface or a low spotlight intensity.

7.0.4 Future Work

During the test with different curvatures, the importance of using a correct radius for the eye during the projection reconstruction becomes apparent. The inclusion of a method to obtain the curvature of the eye beforehand has to be addressed.

Future steps also include the verification of the results using real experiments with realistic eye balls.

List of Figures

3.1	Concept for the spotlight-based Localization with a single Spotlight.	7
3.2	Concept for the spotlight-based Localization with multiple Spotlights.	9
4.1	Cross-section along the optical Axis. Used for the Reconstruction of the Projection.	11
4.2	Example for the constructed Plane.	14
4.3	Triangle (green) used to derive the Vertex Position based on a given Ellipse. .	19
5.1	Blender Scene used to render the Images.	21
5.2	Different Steps of the Contour Detection.	22
6.1	Perpendicular Projection on a Plane.	28
6.2	Angled Projection on a Plane.	30
6.3	Projection on a Sphere.	31
6.4	Path of the Spotlight used during the first Test (Helix).	33
6.5	Reconstructed Positions (green) using one Spotlight for the first Test (Square).	35
6.6	Reconstructed Positions (blue) using three Spotlights for the first Test (Square).	36
6.7	Euclidean Distance between the reconstructed and real Positions for the first Test (Square).	37
6.8	Euclidean Distance between the reconstructed and real Positions separated into the x,y,z Direction. (a) Single Spotlight, (b) Three Spotlights .	38
6.9	Rotational Error of the Prediction. (a) Single Spotlight, (b) Three Spotlights	38
6.10	Path of the Spotlight used during the second Test (Square).	40
6.11	Reconstructed Positions (green) using one Spotlight for the second Test (Helix).	41
6.12	Reconstructed Positions (blue) using three Spotlights for the second Test (Helix).	42
6.13	Euclidean Distance between the reconstructed and reference Positions. .	43
6.14	Euclidean Distance between the reconstructed and reference Positions separated into the x,y and z Direction. (a) Single Spotlight, (b) Three Spotlights	44

List of Figures

6.15 Rotational Error of the Prediction. (a) Single Spotlight, (b) Three Spotlights	45
6.16 Projections using different intensities for the Spotlight.	46
6.17 Average Error of the Prediction for different Intensities.	49
6.18 Maximum Error of the Prediction for different Intensities.	50
6.19 Example for the Impact of the Deformation on the Projection.	52

List of Tables

4.1	The maximum Difference between the Intersections.	16
4.2	Values used for the Calculation of the Maximum Differences.	16
6.1	Ellipse fitted into the Projection onto a Plane (perpendicular).	29
6.2	Values for the Triangle-based Reconstruction (perpendicular).	29
6.3	Ellipse fitted into the Projection onto a Plane (angled).	30
6.4	Values for the Triangle-based Reconstruction (angled).	31
6.5	Ellipse fitted into the reconstructed Projection onto a Sphere.	32
6.6	Values for the Triangle-based Reconstruction (Sphere).	32
6.7	Coordinates of the Points that define the Path for the first Test (Square).	33
6.8	Properties of the Camera in the Blender Simulation.	34
6.9	Positioning Error (Euclidean Distance) for the first Test.	34
6.10	Rotational Error for the first Test.	39
6.11	Positioning Error (Euclidean Distance) for the second Test (Helix).	39
6.12	Rotational Error for the second Test.	44
6.13	Positing Error (euclidean) for different intensities in the first Test using a single Spotlight.	47
6.14	Positing Error (euclidean) for different intensities in the first Test using three Spotlights.	47
6.15	Positing Error (euclidean) for different intensities in the second Test using a single Spotlight.	48
6.16	Positing Error (euclidean) for different intensities in the second Test using three Spotlights.	50
6.17	Positioning Error (Euclidean Distance) for the second Test (Helix) with a deformed Surface.	51
6.18	Positioning Error (Euclidean Distance) for the second Test (Helix) with a wrong Radius.	53

Bibliography

- [1] M. Alsheakhali, A. Eslami, H. Roodaki, and N. Navab. "CRF-based model for instrument detection and pose estimation in retinal microsurgery." In: *Computational and mathematical methods in medicine* 2016 (2016).
- [2] G. Bradski. "The OpenCV Library." In: *Dr. Dobb's Journal of Software Tools* (2000).
- [3] B. O. Community. *Blender - a 3D modelling and rendering package*. Blender Foundation. Stichting Blender Foundation, Amsterdam, 2018.
- [4] Y. Li, W. Zhang, V. P. Nguyen, R. Rosen, X. Wang, X. Xia, and Y. M. Paulus. "Real-time OCT guidance and multimodal imaging monitoring of subretinal injection induced choroidal neovascularization in rabbit eyes." In: *Experimental eye research* 186 (2019), p. 107714.
- [5] W. H. Organization. *World report on vision*. Tech. rep. World Health Organization, 2019.
- [6] T. Probst, K.-K. Maninis, A. Chhatkuli, M. Ourak, E. Vander Poorten, and L. Van Gool. "Automatic tool landmark detection for stereo vision in robot-assisted retinal surgery." In: *IEEE Robotics and Automation Letters* 3.1 (2017), pp. 612–619.
- [7] N. Rieke, D. J. Tan, M. Alsheakhali, F. Tombari, C. A. di San Filippo, V. Belagiannis, A. Eslami, and N. Navab. "Surgical Tool Tracking and Pose Estimation in Retinal Microsurgery." In: *Medical Image Computing and Computer-Assisted Intervention – MICCAI 2015*. Ed. by N. Navab, J. Hornegger, W. M. Wells, and A. Frangi. Cham: Springer International Publishing, 2015, pp. 266–273. ISBN: 978-3-319-24553-9.
- [8] N. Rieke, D. J. Tan, C. A. di San Filippo, F. Tombari, M. Alsheakhali, V. Belagiannis, A. Eslami, and N. Navab. "Real-time localization of articulated surgical instruments in retinal microsurgery." In: *Medical image analysis* 34 (2016), pp. 82–100.
- [9] A. Routray, R. A. MacLachlan, J. N. Martel, and C. N. Riviere. "Real-Time Incremental Estimation of Retinal Surface Using Laser Aiming Beam." In: *2019 International Symposium on Medical Robotics (ISMR)*. 2019, pp. 1–5.

Bibliography

- [10] A. Üneri, M. A. Balicki, J. Handa, P. Gehlbach, R. H. Taylor, and I. Iordachita. "New steady-hand Eye Robot with micro-force sensing for vitreoretinal surgery." In: *2010 3rd IEEE RAS EMBS International Conference on Biomedical Robotics and Biomechatronics*. 2010, pp. 814–819.
- [11] G. Van Rossum and F. L. Drake. *Python 3 Reference Manual*. Scotts Valley, CA: CreateSpace, 2009. ISBN: 1441412697.
- [12] P. K. Verkiculara, A. Mathur, E. A. Mallen, J. M. Pope, and D. A. Atchison. "Eye shape and retinal shape, and their relation to peripheral refraction." In: *Ophthalmic and Physiological Optics* 32.3 (2012), pp. 184–199.
- [13] Q. Wu, D. Xu, and W. Zou. "A survey on three-dimensional modeling based on line structured light scanner." In: *Proceedings of the 33rd Chinese Control Conference*. 2014, pp. 7439–7444.
- [14] G.-Z. Yang, J. Cambias, K. Cleary, E. Daimler, J. Drake, P. E. Dupont, N. Hata, P. Kazanzides, S. Martel, R. V. Patel, V. J. Santos, and R. H. Taylor. "Medical robotics—Regulatory, ethical, and legal considerations for increasing levels of autonomy." In: *Science Robotics* 2.4 (2017). doi: 10.1126/scirobotics.aam8638. eprint: <https://robotics.sciencemag.org/content/2/4/eaam8638.full.pdf>.
- [15] S. Yang, M. Balicki, R. A. MacLachlan, X. Liu, J. U. Kang, R. H. Taylor, and C. N. Riviere. "Optical coherence tomography scanning with a handheld vitreoretinal micromanipulator." In: *2012 Annual International Conference of the IEEE Engineering in Medicine and Biology Society*. 2012, pp. 948–951.
- [16] S. Yang, J. N. Martel, L. A. Lobes Jr, and C. N. Riviere. "Techniques for robot-aided intraocular surgery using monocular vision." In: *The International journal of robotics research* 37.8 (2018), pp. 931–952.
- [17] H. Yu, J. Shen, K. M. Joos, and N. Simaan. "Design, calibration and preliminary testing of a robotic telemanipulator for OCT guided retinal surgery." In: *2013 IEEE International Conference on Robotics and Automation*. 2013, pp. 225–231.
- [18] M. Zhou, X. Hao, A. Eslami, K. Huang, C. Cai, C. P. Lohmann, N. Navab, A. Knoll, and M. A. Nasseri. "6DOF needle pose estimation for robot-assisted vitreoretinal surgery." In: *IEEE Access* 7 (2019), pp. 63113–63122.
- [19] M. Zhou, K. Huang, A. Eslami, H. Roodaki, D. Zapp, M. Maier, C. P. Lohmann, A. Knoll, and M. A. Nasseri. "Precision needle tip localization using optical coherence tomography images for subretinal injection." In: *2018 IEEE International Conference on Robotics and Automation (ICRA)*. IEEE. 2018, pp. 1–8.

Bibliography

- [20] M. Zhou, H. Roodaki, A. Eslami, G. Chen, K. Huang, M. Maier, C. P. Lohmann, A. Knoll, and M. A. Nasseri. "Needle segmentation in volumetric optical coherence tomography images for ophthalmic microsurgery." In: *Applied Sciences* 7.8 (2017), p. 748.
- [21] M. Zhou, X. Wang, J. Weiss, A. Eslami, K. Huang, M. Maier, C. P. Lohmann, N. Navab, A. Knoll, and M. A. Nasseri. "Needle Localization for Robot-assisted Subretinal Injection based on Deep Learning." In: *2019 International Conference on Robotics and Automation (ICRA)*. IEEE. 2019, pp. 8727–8732.
- [22] M. Zhou, J. Wu, A. Ebrahimi, N. Patel, C. He, P. Gehlbach, R. H. Taylor, A. Knoll, M. A. Nasseri, and I. I. Iordachita. "Spotlight-based 3D Instrument Guidance for Retinal Surgery." In: *2020 International Symposium on Medical Robotics (ISMR)*. May 2020.